Force and Hydrodynamic Efficiency Measurements of a Three-Dimensional Flapping Foil

by

Karl-Magnus Weidmann McLetchie

Submitted to the Department of Ocean Engineering and the
Department of Mechanical Engineering
in partial fulfillment of the requirements for the degree of
Masters of Science in Ocean Engineering

and

Masters of Science in Mechanical Engineering
at the
MASSACHUSETTS INSTITUTE OF TECHNOLOGY
May 2004 [June 2004]

Author . . . . , ...
Department of Ocean Engineering and the Department of Mechanical
Engineering
May 26, 2004
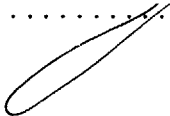
Certified by . . . .
Michael S. Triantafyllou
Professor of Ocean Engineering
Thesis Supervisor

Certified by . . . .
Douglas P. Hart
Professor of Mechanical Engineering
Thesis Supervisor
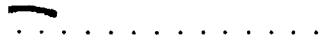
Accepted by . . . .
Michael S. Triantafyllou
Chairman, Department Committee on Graduate Students,
Ocean Engineering
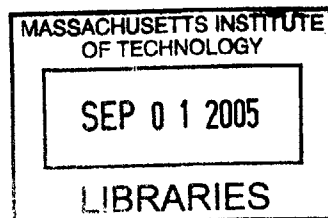
Accepted by . . . .
Ain Sonin
Chairman, Department Committee on Graduate Students,
Mechanical Engineering

Force and Hydrodynamic Efficiency Measurements of a Three-Dimensional Flapping Foil

by

Karl-Magnus Weidmann McLetchie

Abstract

Investigations into unsteady flapping foil propulsion have shown that it is an efficient and high thrust means of propulsion. Extensive work has been done to optimize the efficiency of two-dimensional flapping foils, varying both the kinematics of the motion and the flexibility of the foil. However, no thorough investigation into the hydrodynamic efficiency of three-dimensional flapping foils has been made.

In this thesis, experimental hydrodynamic efficiency measurements and force measurements of a three-dimensional flapping foil are presented. These measurements were made by mounting a small, six-axis dynamometer directly onto the foil shaft of a flapping foil module. The module uses two computer controlled servo motors to actuate a foil in a sinusoidal pitch and roll motion, similar to the motion of a penguin's wing.

The measured thrust coefficients compared well to previous experimental results, and the on-shaft dynamometer proved to be a valuable sensor. However, the experimental apparatus must be modified before reliable efficiency results can be made for the entire range of kinematics. Once these improvements are made, a thorough investigation into the effects of foil geometry and flexibility can be done to find the optimum efficiency parameters of a three-dimensional flapping foil. These optimum efficiency parameters will be valuable for the development of flapping foil vehicles.

Thesis Supervisor: Michael S. Triantafyllou
Title: Professor of Ocean Engineering

Thesis Supervisor: Douglas P. Hart
Title: Professor of Mechanical Engineering

Acknowledgments

I would like to thank Professor Triantafyllou and Dr. Franz Hover for their their guidance and support. Also, Professor Hart for reviewing my thesis with such short notice.

I would like to thank Professor Techet and Ben Connell for taking time out of their work to help me through my many flapping foil problems.

I would like to thank everyone in the towtank that has worked with me down there over the past six years, David Beal, Craig Martin, Joshua Tolford Davis, Anna Pauline Miranda Michel, Øyvind Smogeli, Victor Polidoro, Stephen Licht, Prada Prempraneerach, Jason Dahl, and Andrew Wiggins. All of you have been good friends, and made the towtank a good place to work.

Special thanks to Fred Cote for teaching me how to machine and giving me useful advice on all of my projects.

Skål til Norge.

Contents

List of Figures

List of Tables

Chapter 1

Introduction

1.1 Biological Motivation

Over millions of years many aquatic animals have adapted to use flapping foils as their main means of propulsion. These animals, including sea lions, sea turtles, penguins, and pectoral swimming fish are just as fast and agile as most tail swimming fish and far more agile than any man-made underwater vehicle.

Figure 1-1 shows the classification of flapping foil animals and the timeline of their evolution. The dates placed next to each class represent the approximate date that the particular class split off from their common ancestor in the sub-phylum vertebrata [7]. Although the split of these classes occurred over hundreds of millions of years, all the animals evolved fins with similar geometries and kinematics. All of their fins have streamlined cross sections, approximately three to one aspect ratios, and oscillate to produce lift-based propulsion.

In this thesis, the force production and hydrodynamic efficiency of a three dimensional flapping foil are investigated using a robotic flapping foil actuator. The actuator attempts to mimic the kinematics of biological flapping foil swimmers, and the foil has a planform and cross section similar to that of a penguin's wing.

A six-axis dynamometer is used to measure all of the forces and moments generated by an unsteady, three-dimensional flapping foil.

The Classification and Evolution of Flapping Foil Animals

Domain - Eukarya

　　└─►**Kingdom** - Animalia

　　　　└─►**Phylum** - Chordata

　　　　　　└─► **Sub-Phylum** - Vertebrata

　　　　　420 Million BC ──► Class Actinopterygii - ie wrasse fish

　　　　　300 Million BC ──► Class Reptilia - ie sea turtles

　　　　　200 Million BC ──► Class Mamalia - ie whales and sea lions

　　　　　150 Million BC ──► Class Aves - ie penguins
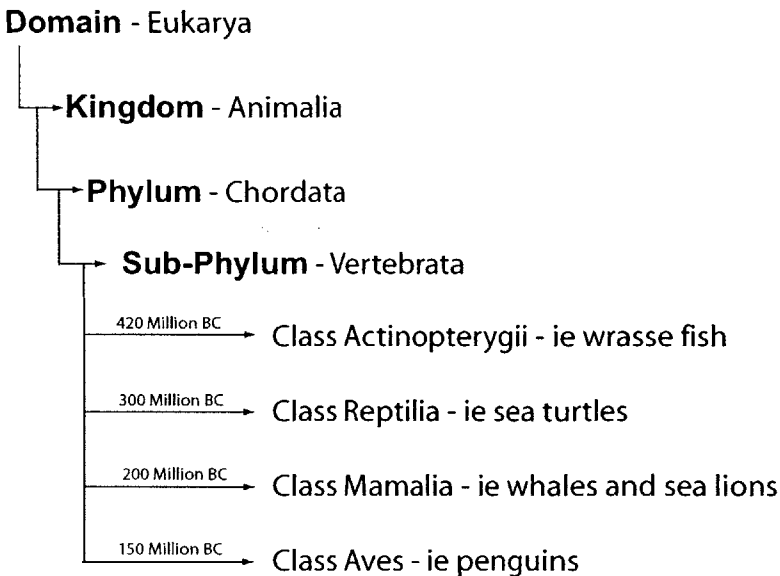
Figure 1-1: .
The classification of flapping foil animals and the timeline of their evolution. The dates represent approximate times that the class split off from the common ancestor
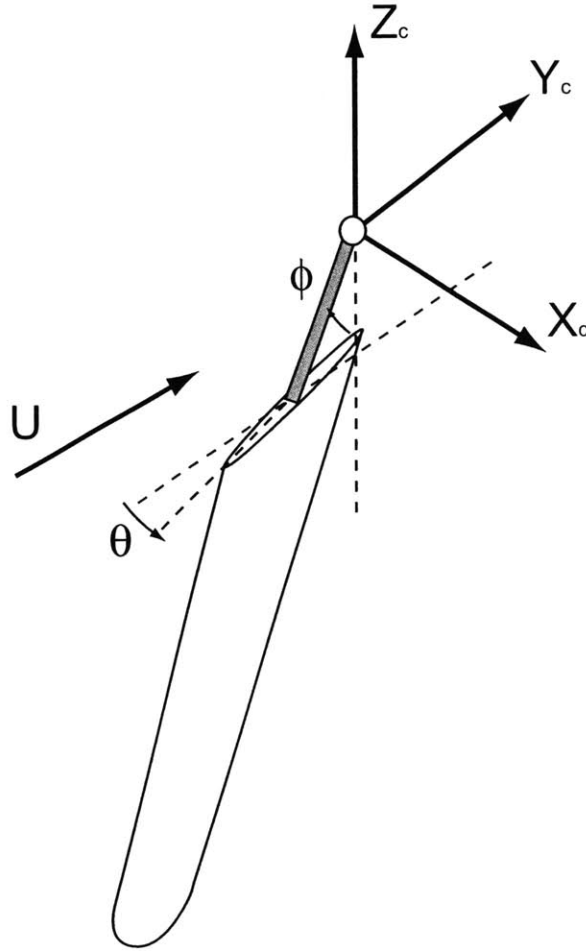
Figure 1-2: .
A three-dimensional view of the flapping foil with carriage coordinate conventions
and angle conventions

1.2 Foil Kinematics and Sign Conventions

Over the years of testing flapping foils, different sign conventions and angle definitions
have been used to describe the kinematics of a flapping foil. In this thesis, a right
handed coordinate system, fixed to the moving carriage, is used with the y-axis aligned
with the flow and the z-axis pointing upwards. All angles and moments are defined
as positive in the right-handed sense.

Figure 1-2 shows a schematic of the sign conventions used to describe the foil
kinematics. The origin of the carriage coordinate system $[x_{co}, y_{co}, z_{co}]$ is at the center
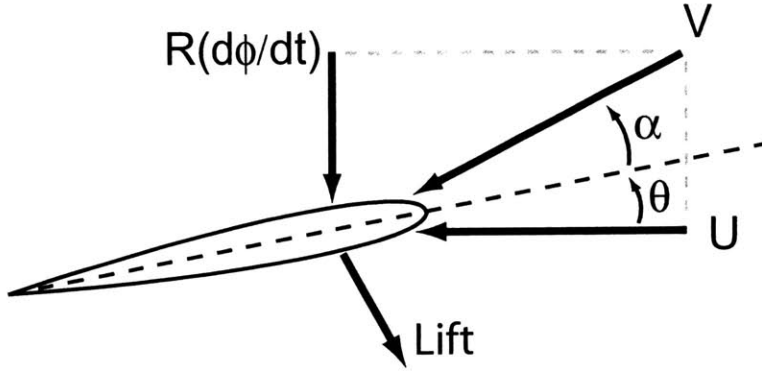
Figure 1-3: The velocity vectors and definition of $\alpha(t)$

of rotational motion. The foil "rolls" about the origin with an angular position, $\phi(t)$, and "pitches" about the origin with an angular position, $\theta(t)$. The equations of these positions are:

$$\phi(t) = -\phi_o sin(\omega t) \qquad (1.1)$$

$$\theta(t) = \theta_o sin(\omega t + \psi) \qquad (1.2)$$

where ω is the flapping frequency, ψ is the phase angle, and ϕ_o and θ_o are the roll and pitch amplitudes, respectively.

A phase angle, ψ, of $\pi/2$ was always used, so equation 1.2 simplifies to.

$$\theta(t) = \theta_o cos(\omega t) \qquad (1.3)$$

These sinusoidal motions with a phase difference of $\pi/2$ were chosen because they lead to good thrust production and efficiency [12].

At each radius, r, from the origin, the cross section of the foil has a different

16
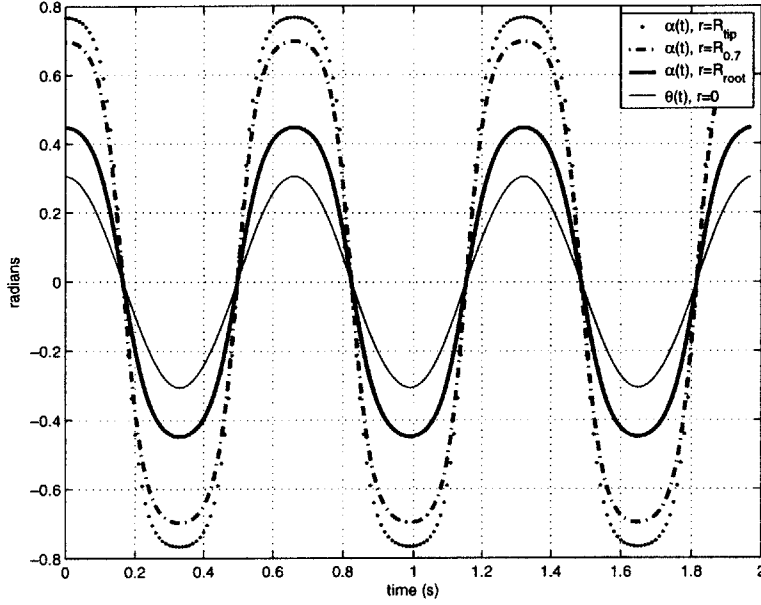
Figure 1-4: $\alpha(t)$ and $\theta(t)$ plotted verses time for the case of f=1.515Hz, $\phi_o = 11^o$ and $\theta_o = 17.5^o$. This corresponds to $\alpha_{max} = 40^o$, $h_o/c = 1.5$, and St=0.5

angular velocity and angle of attack to the uniform incoming flow. Figure 1-3 shows a diagram of a cross section of the foil at a radius, R, from the origin. This cross section sees two different fluid velocities; one from the uniform flow, U, and one from the roll velocity, $R\dot{\phi}(t)$. The vector addition of these two velocities is the apparent velocity seen by the foil, V. The foil has an angle of attack, $\alpha(t)$, to the apparent velocity defined as:

$$\alpha(t) = \arctan\left(\frac{r\phi_o\omega\cos(\omega t)}{U}\right) - \theta_o\cos(\omega t) \tag{1.4}$$

An oversimplified, but illustrative explanation of flapping foil thrust production looks at the lift forces on a single cross section of the foil. This 2-D cross section of the foil produces a lift force that is perpendicular to the apparent velocity, V. When $\alpha(t)$ has the same sign as $\theta(t)$, the lift vector has a component in the opposite direction of the flow, producing a thrust. If enough of the sections produce this thrust, then they integrate along the span of the foil to produce a net thrust in the carriage frame.

The angle of attack at any point in time varies with the radius. Figure 1-4 plots

17
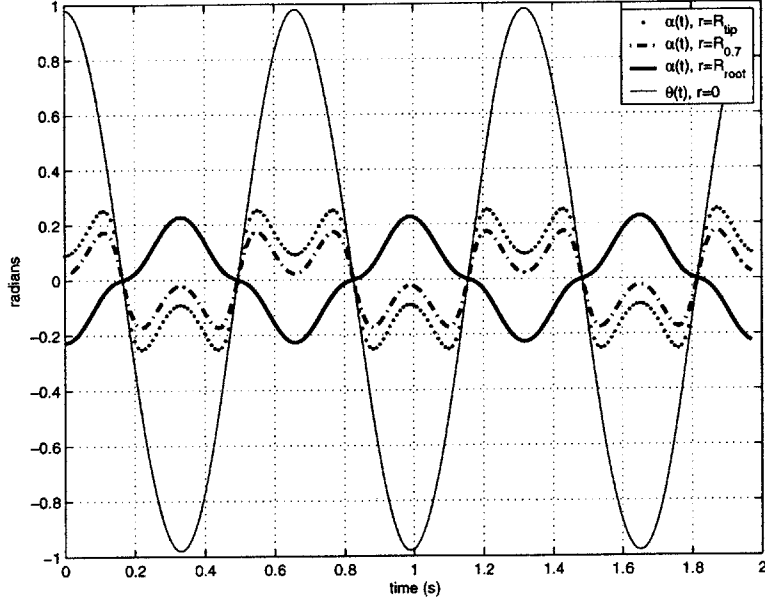
Figure 1-5: $\alpha(t)$ and $\theta(t)$ plotted verses time for the case of f=1.515Hz, $\phi_o = 11^o$, and $\theta_o = 56.2^o$. This corresponds to $\alpha_{max} = 10^o$, $h_o/c = 1.5$, and St=0.5

the angle of attack through time at different radii for a set of kinematics. At the tip of the foil, the amplitude of $\alpha(t)$ is greatest, while at the center of roll it goes to $\theta(t)$. Because the sign of $\alpha(t)$ is always the same as $\theta(t)$, this particular case produces significant thrust.

Figure 1-5 plots the angle of attack at different radii for a set of kinematics that did not produce significant thrust. Note that the angle of attack amplitude is small and its sign is opposite of the pitch sign near the root of the foil.

1.3   Dimensionless Parameters

The dimensionless parameters of maximum angle of attack, α_{max}, heave amplitude, $h_{0.7}/c$, and Strouhal number, St, define the foil kinematics for all tests.

All three of these parameters are defined at a radius that is 70% of the foil span, $R_{0.7}$.

18

$$R_{0.7} = R_r + 0.7S, \tag{1.5}$$

where R_r is the distance from the center of roll to the foil root and S is the foil span. This radius is chosen because it is assumed to be the center of force of a three-dimensional flapping foil. This assumption will be investigated later in the thesis.

The maximum angle of attack, calculated at $R_{0.7}$, over one period, T, is defined as:

$$\alpha_{max} = max\{\alpha(t)\} \tag{1.6}$$

The non-dimensional swept arclength, called the heave amplitude, is defined as:

$$h_{0.7}/c = R_{0.7}\phi_o/c \tag{1.7}$$

where c is the average chord of the foil.

The Strouhal number for the three dimensional flapping foil is defined as:

$$St = \frac{2h_{0.7}f}{U} \tag{1.8}$$

where f is the flapping frequency and U is the flow velocity. $2h_{0.7}$ was chosen as an an estimate of the width of the foil wake at $R_{0.7}$.

To reach the desired St, α_{max}, and h_o/c for a given test, the flapping frequency, roll amplitude, and pitch amplitude were varied.

All of the tests were run at a Reynolds number of 27,500 based on the uniform flow velocity and the average foil chord.

1.4   Previous Work

This thesis documents the first attempt to measure the hydrodynamic efficiency of a three-dimensional flapping foil. However, extensive research has already been done to measure the hydrodynamic efficiency and force production of two-dimensional flap-

19

ping foils. Extensive work has also been done to measure the force production of three-dimensional flapping foils.

1.4.1 Two-Dimensional Flapping Foils

A two-dimensional flapping foil is heaved transversely to the flow and pitched to adjust its angle of attack. This motion produces two-dimensional flow at each cross-section along the span of the foil. For experimental testing, a rectangular planform, high aspect ratio foil is used, and neglecting end effects, the flow around the foil is considered two-dimensional.

McGregor [11] did some early experimental investigations into flapping foil propulsion. The foil was attached to a flexible bar and oscillated sinusoidally with a single degree of freedom, mimicking the motion of a fish tail. A maximum efficiency of 0.7 was recorded in these experiments.

Anderson [1] began the tradition of flapping foil research at the MIT Towing tank by measuring the thrust and efficiency of a rigid, two-dimensional flapping foil, and by using digital particle image velocimetry (DPIV) to measure the flow around the foil. She measured a maximum efficiency of 0.87 under the optimal wake conditions recorded by the DPIV.

Read [12] continued this work, by using a new mechanism that allowed independent computer control of the pitch and heave motions. He commanded sinusiodal motions, and by varying the phase angle, ψ, found an optimal ψ of $\pi/2$. At this phase angle He found a peak thrust coefficient of 2.1 and a peak efficiency of 0.7.

Haugsdal [4] improved the performance of rigid, two-dimensional flapping foils by commanding specific angle of attack profiles. He commanded square profiles, saw-tooth profiles, and cosine profiles. He found that the saw-tooth profiles led to a maximum thrust coefficient of 3, while the cosine profiles led to a maximum efficiency of 0.64.

Prempraneerach [8] continued to optimize the performance of two-dimensional flapping foils by varying the chordwise flexibility of the foil. He found that introducing chordwise flexibility reduced thrust production, but increased efficiency by up to 25%.

20

Pedro [3] computationally solved the flow around a two-dimensional pitching and heaving hydrofoil. For tests at $Re = 11000$, he found an efficiency peak of 0.64, which is lower than the experimental results. He attributes the discrepancy to the low Reynolds Number used in the computations. At this low Reynolds number, the viscous forces are relatively large compared to the thrust and lift forces, so the efficiency is lower.

1.4.2 Three-Dimensional Flapping Foils

At MIT, experimental work has been done with high aspect ratio, three-dimensional flapping foils that mimic the geometry and kinematics of penguin wings and sea turtle flippers. Flores [2] measured the thrust force produced by a symmetrically flapping foil, and the lift force produced by a foil flapped with a bias angle. She measured a maximum thrust coefficient of 2 for the symmetrically flapping foil and a maximum lift coefficient of 3.5 with a bias angle of 30°. This lift coefficient is seven times higher than the static stall lift coefficient of the same foil.

Polidoro [9] tested flapping foils of different aspect ratios, and found that an aspect ratio of four led to the highest thrust coefficient. This aspect ratio is consistent with most three-dimensional flapping foils found in nature.

Slicht [13] has applied Flores and Polidoro's research to building and developing the control system for a flapping foil AUV. This AUV has four independantly controlled flapping foils, arranged in a configuration similar to the flippers of a sea turtle. The vehicle is currently being tested.

Kato [5] has done extensive experimental work analyzing the performance of low aspect ratio flapping foils. These foils mimic the geometry and kinematics of pectoral swimming fish. He has applied this experimental work to the development of a flapping foil AUV that can swim a prearranged course and hover in water currents.

Ramamurti [10] used a finite element flow solver to computationally solve for the flow around a three-dimensional insect wing. His thrust and lift results compared well to experimental data taken experimentally.

1.5 Goals of The Thesis

This thesis has three goals, to:

- Implement a new sensor and crosscheck its performance against past force measurements.

- Measure the hydrodynamic efficiency of a three-dimensional flapping foil.

- Find the center of force on a flapping foil under different kinematic conditions.

Implementing the six-axis dynamometer on a foil shaft that has two degrees of freedom was the first goal. The mounting techniques, calibration methods, and angle transformations developed will be valuable to future users. Comparing the force data to previous force data will validate both the old and new results.

By measuring the hydrodynamic efficiency of the flapping foil, a general idea of how St, h_o/c, and α_{max} effect efficiency was recorded. Past experiments with three-dimensional flapping foils have measured the efficiency of the motors that drive the foils [9], however this measurement relies on the characteristics of the particular motors used, and becomes useless if the motors are changed. The hydrodynamic efficiency measurement allows vehicle designers to choose motors and foil kinematics based on the optimal hydrodynamic efficiency and thrust conditions.

In the past, the center of force of a flapping foil was assumed to be at 70% of the foils span. This distance, $R_{0.7}$, is incorporated into all of the dimensionless parameters. Using the on-shaft dynamometer the actual radius of the center of force can be measured and used for future actuator design and vehicle control. Also, knowing the center of force allows CFD and PDIV analysis to be performed at the most important spanwise positions.

Chapter 2

Experimental Apparatus and Methods

This chapter gives an overview of the structure and control of the flapping foil module. It also gives a detailed description of the potentiometer and dynamometer used to measure the foil position and forces, respectively.

All of the tests were run in the MIT towing tank, a 30m long, 2.5m wide, 1.2m deep rectangular testing tank. The main towing carriage was used to tow the experimental apparatus at a constant velocity of 0.5m/s down the tank.

All force and position data were recorded at 500Hz by a 16 channel, 12 bit data acquisition card located on a computer in the towtank bridge.

Figure 2-1 shows a schematic of the entire test apparatus. All of the parts identified in the figure and shown in Figure 2-2 are described in the following sections.

2.1 Flapping Foil Module

The flapping foil module used for the experiments was designed to be one of four actuators on a flapping foil AUV. The module was removed from the AUV and modified to mount to the towtank carriage. For a detailed description of the design and construction of the module refer to Polidoro's thesis [9].
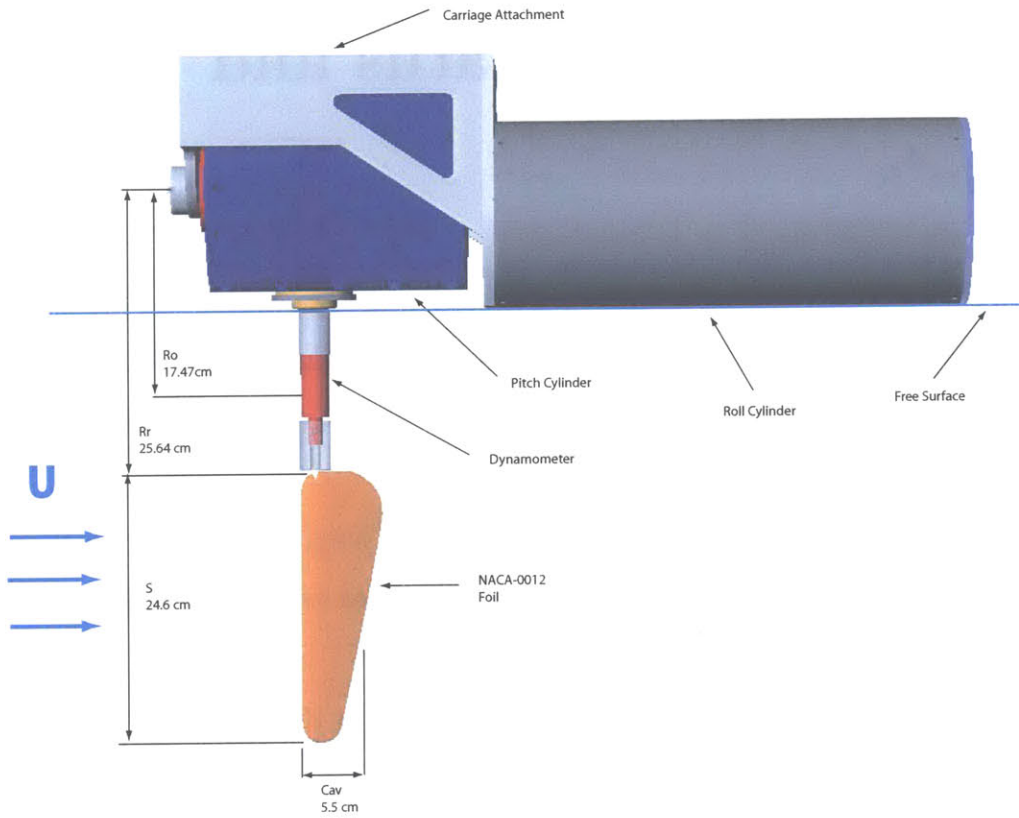
23

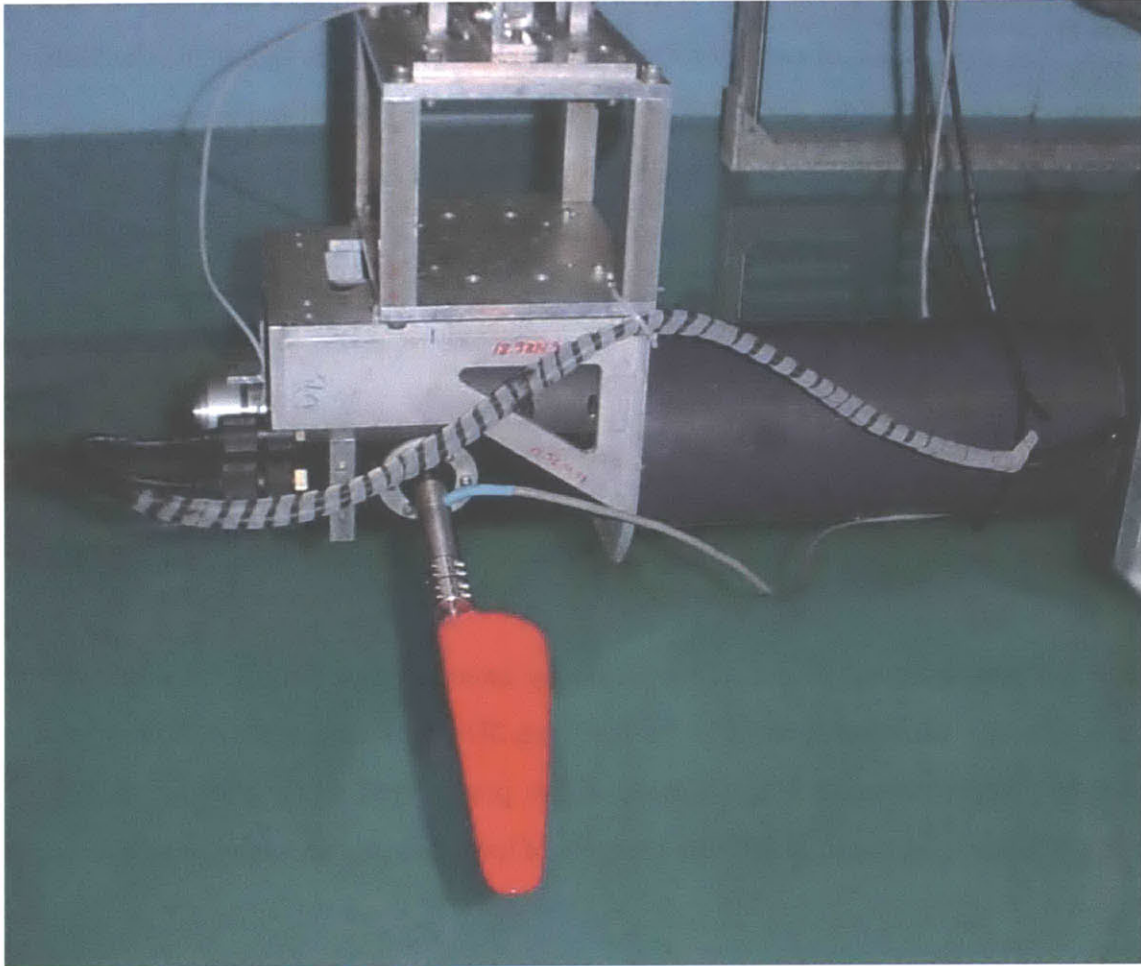Figure 2-1: A side view of the module taken from a CAD drawing.

Figure 2-2: A photo of the module; note that the foil is rolled out of the water.

2.1.1   Module Control

The two degrees of actuation, pitch and roll, are provided by two electric DC motors. These motors run off of amps that are controlled by a dual axis Galil motor control card (Galil Motion Control Inc, Rocklin, CA). The card is commanded via wireless ethernet by the user in the bridge of the towtank.

To home the module to the same zero position at the beginning of each day, optical switches were used inside of each housing. These switches output signals to the Galil card and a homing routine, downloaded to the Galil card, homed both axes.

The module control code, developed by Stephen Licht, allows the user to input a flapping frequency, pitch amplitude, and roll amplitude to command the sinusoidal motion of the two axes.

2.1.2   The Foil

The foil used in the experiments is a tapered 24.6cm span, 5.5cm average span foil with a NACA-0012 cross section. The same foil mold was used by Martin [6] and Flores [2] in their experiments.

The foil was designed in a CAD program by sweeping the NACA cross sections along the linearly tapering span. The foil was then 3D printed using stereolithography (Protocam, Northhampton, PA). A mold of the printed foil was made out of RTV molding silicone, and the final foil was cast out of low viscosity urethane in this mold.

2.2   The Potentiometer

To measure the roll position, a potentiometer was placed externally to the roll cylinder, above the surface of the water. A potentiometer could not be placed on the pitch axis because this would be below the water. In future models of the module, there will be a potentiometer both inside the roll cylinder and inside the pitch cylinder.

The potentiometer used was an Inscale GL-200 hollow shaft potentiometer (Inscale, East Sussex, UK). This potentiometer has a linearity of $+/-0.25\%$ and a

repeatability of 0.1^o

The shaft sleeve of the potentiometer has infinite rotation, so an error in the motor code will not break it (note: this infinite rotation was a specific modification by Inscale, and normal GL-200 can only rotate 346° before breaking). An input voltage of 5V was used to power the potentiometer, resulting in an output a voltage of 0.0139 V/degree.

To estimate the pitch position during data analysis, the recorded roll position was shifted by $\pi/2$ radians and scaled to the appropriate amplitude. This simplifying step was taken for several reasons:

- A potentiometer couldn't fit in the pitch canister.

- The output of the pitch encoder couldn't be reliably recorded over a full run.

- The pitch position couldn't be estimated as a sinusoid during the data analysis because a slight error in the frequency estimation would put it out of phase with the force data. For example, a 1% error in frequency estimation would lead to a 20% error in phase by the end of a 20 cycle long data sequence.

An error limit of 2° was imposed in the motor control code of both the pitch and roll axes. To insure that the the positions were being commanded correctly, the output of the pitch and roll encoders were periodically checked. The positions were always within 2% of the commanded sinusoidal positions, and the pitch always had the correct phase relative to the roll.

Figure 2-3 shows the plot of angular positions and velocities for a run of the foil. The positions are measured and calculated as described above, then filtered with a 3rd order, 7Hz cuttoff, butterworth filter. The velocities are the numerical derivatives of the positions.

2.3 The Dynamometer

All of the force and torque measurements were made using a single dynamometer, the AMTI MCI-6-250 (Advanced Mechanical Technology, INC, Watertown, MA). The
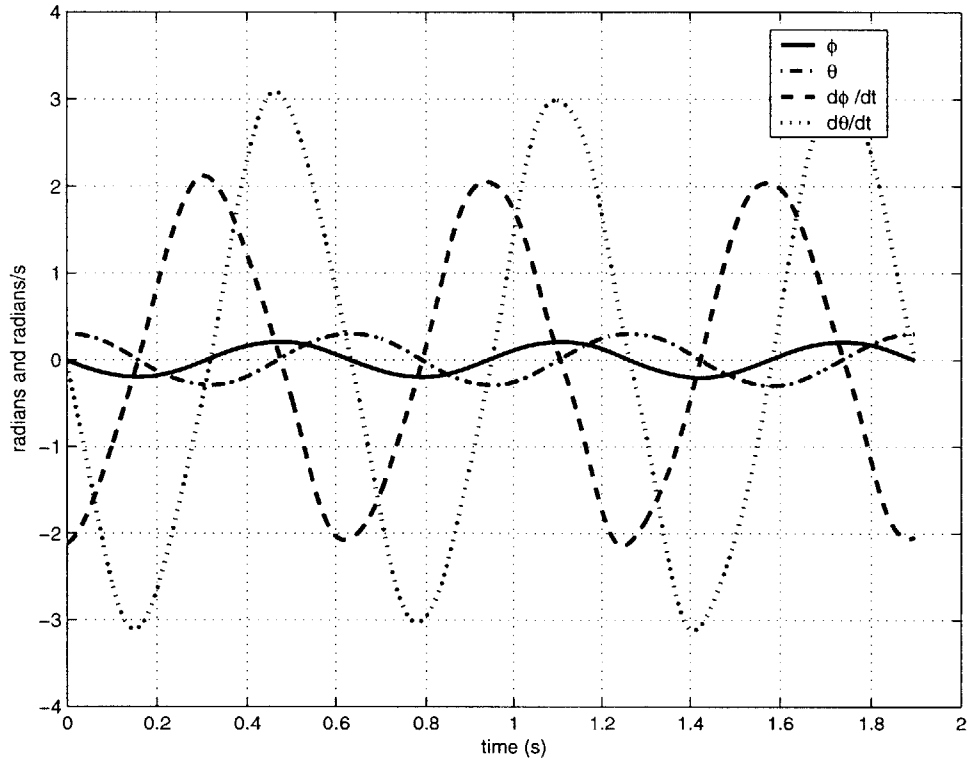
Figure 2-3: A plot of the angular positions and velocities for $\theta_o = 17.5^o(0.3rad)$, $\phi_o = 11^o(0.2rad)$, and f=1.5 Hz (9.4 rad/s)
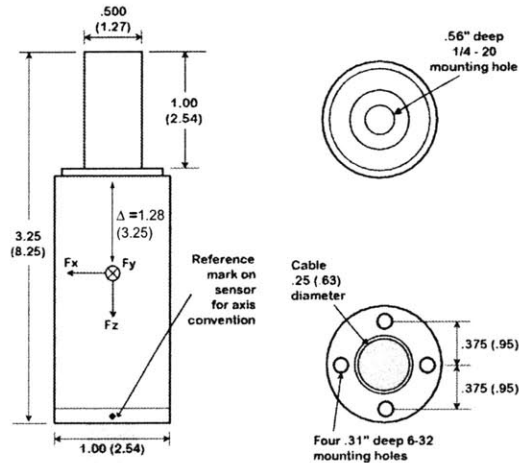
Figure 2-4: A diagram of the MCI-6 showing dimensions

MCI-6-250 is a waterproof, six axis strain gauge force transducer, with a maximum F_z capacity of 250lbs. A 500 lb model is also available. Figure 2-4 is a drawing of the MC1-6 with its dimensions and mounting holes labeled. The distance from the edge of the dynamometer body to the center of moment is labeled as $\Delta = 3.25cm$. This dimension is supplied by the factory and used in all future moment calculations.

A stainless steel couple was designed and machined to connect the base of the dynamometer to the module shaft. One end of this couple fit over the signal cable and bolted to the four mounting holes; while the other end was pinned to the foil shaft. To attach the dynamometer head to the foil shaft, an off the shelf clamping shaft couple was used.

The signals from the dynamometer were amplified with an AMTI MCA-6 amplifier. This amplifier outputs a common excitation voltage of 2.5 V, 5V, or 10 V +/-0.01 V as specified by the user. It then amplifies the six outputs from the sensor with independent gain and filtering settings for each channel. The gain can be set to 1000, 2000, or 4000 and the filtering can be set to a 10.5 Hz or 1050Hz second order critically damped low-pass filter.

Table 2.1 summarizes the amplifier settings used, and gives the factory supplied

29

Channel	V_{ex}	Gain	Filter	Capacity	sensitivity	sensitivity
F_x	10 V	4000	1050Hz	556N	$1.567 \mu V/V_{ex} N$	0.0627 V/N
F_y	10 V	4000	1050Hz	556N	$1.564 \mu V/V_{ex} N$	0.0626 V/N
F_z	10 V	4000	1050Hz	1112N	$0.393 \mu V/V_{ex} N$	0.0157 V/N
M_x	10 V	1000	1050Hz	5.65Nm	$119.6 \mu V/V_{ex} Nm$	1.196 V/Nm
M_y	10 V	1000	1050Hz	5.65Nm	$120.7 \mu V/V_{ex} Nm$	1.196 V/Nm
M_z	10 V	1000	1050Hz	5.65Nm	$121.8 \mu V/V_{ex} Nm$	4.871 V/Nm

Table 2.1: The settings of the amplifier, factory supplied sensitivities, and amplified sensitivities.

rated capacities and sensitivities. The last column in the table shows the actual sensitivities after adjusting for the gain and excitation voltage.

The rated capacities have an engineering design factor of two for a load supplied to a single axis, and a lower design factor for loads applied to multiple axes. To be safe, the rated loads were treated as the breaking loads and never exceeded.

2.3.1 Calibration

Before and after every group of tests, all six axes of the dynamometer were calibrated. This calibration served to verify the factory supplied sensitivities, and to ensure that the dynamometer was working properly on that day.

To perform the calibration, a pulley rig was made out of 80/20 T-slotted aluminum (80/20 Inc., Columbia City, IN). The rig was bolted to the carriage to ensure that it was properly aligned with the carriage coordinate system. The dynamometer was then aligned with the carriage coordinate system by homing the pitch and roll axes with the optical switches. When the motors are left on, the foil shaft remains rigidly at this zeroed position.

Figure 2-5 shows the sign convention of the dynamometer.

To calibrate each axis, a series of weights were hung from the pulley rig and a cord was directed to apply the force in the appropriate direction. The weights used were W=[0.383 1.109 1.290 2.016 2.923 3.830] kg. These applied a range of force from 3.75N to 37.5 N for all of the force calibrations.

To calibrate F_x, the force was applied as close the center of moment as possible
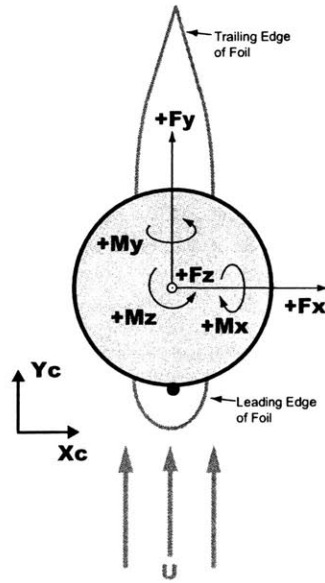
Figure 2-5: Sign convention of the dynamometer, viewed from above.

(3.25 cm, as shown in Figure 2-4) The force applied in the x-direction also caused a moment in the y-direction. To calibrate F_y, the dyno was pitched $\theta = 90^o$ and the process was repeated.

To calibrate F_z the pulley system was arranged so that the cord pulled straight down on the dyno, applying the force with no applied moments.

To calibrate M_x and M_y, the data from the F_x and F_y calibrations could be used, assuming a lever arm of 3.25cm. However, to do a geometrically different calibration, the pulleys were moved down to increase the lever arm to 8cm. The applied moment range was then 0.3Nm to 3Nm.

Finally, to calibrate M_z a bolt was screwed into the stainless steel foil couple perpendicularly to the foil shaft in the y-direction. The force was then applied perpendicularly to this bolt at a distance of 6.35 cm from the z-axis. The range of applied moments was then 0.238Nm to 2.38Nm. When this M_z was applied an F_x and an M_y were also applied.

Figure 2-6 shows the raw data taken from the F_x channel for the F_x and M_y calibration. While the first six weights were applied, the force was applied 3.25cm from the center of moment, and for the last six it was applied 8cm from the center
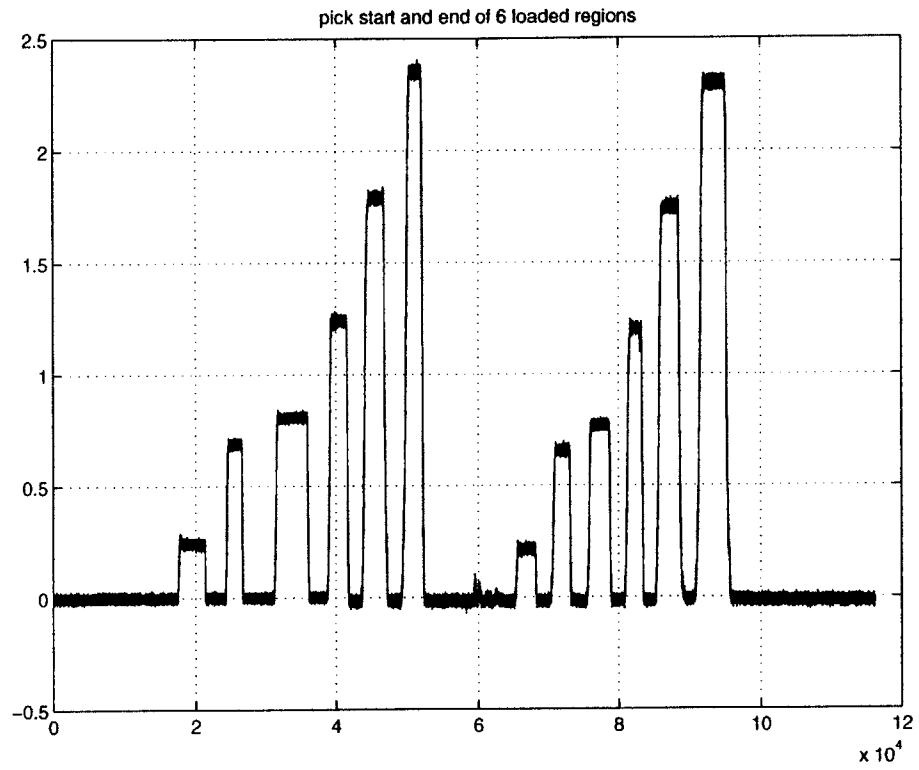
Figure 2-6: The raw data from the F_x calibration. The vertical axis is in volts, and the horizontal in samples.
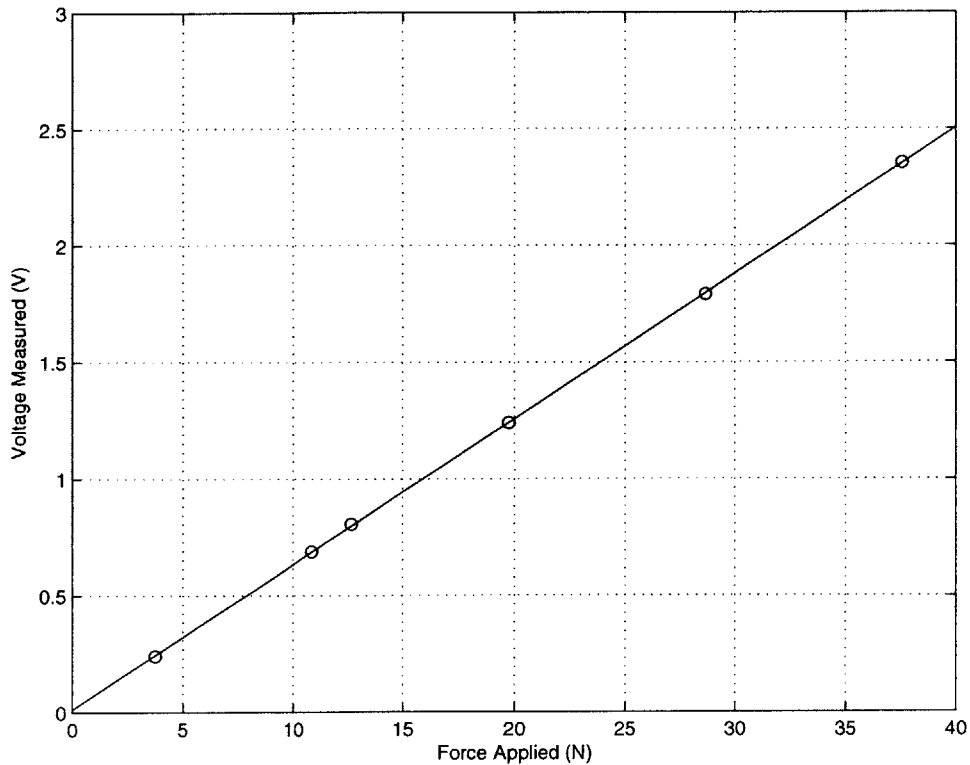
Figure 2-7: The linear fit to the F_x calibration. The slope of this line is 0.0623V/N, just 0.63% lower than the factory sensitivity of 0.0627 V/N.

of moment. Notice that the force signal does not change significantly based on the length of the moment arm.

Figure 2-7 shows the linear fit to the raw data of Figure 2-6. For every channel, the calibration was linear, and the slope of the linear fit was always within 3% of the factory supplied sensitivities shown in Table 2.3. These slopes became the diagonal entries in the full sensitivity matrix.

2.3.2 Crosstalk

The MC1 sensor is advertised to have less than 2% crosstalk on all channels. This statement means that if a signal of 10V is output by one channel, electrical interference could cause an output of 0.2V on another channel. This 2% crosstalk could be significant because the lift forces produced by a flapping foil are often an order of

magnitude greater than the thrust forces. Therefore the thrust force measurement could be significantly affected by the lift force measurement.

The calibrations performed with the sensor mounted to the module were insufficient to measure crosstalk because the roll gearhead has 1.5^o backlash and the pitch gearhead has 2.5^o of backlash. This backlash makes it impossible to differentiate the crosstalk from angular misalignments. If the dynamomoter is pitched 2.5^o out of alignment and a calibration weight, W, is applied in the x-direction of the carriage, then the F_x channel will read:

$$F_x = W cos(\theta) = 0.999W \tag{2.1}$$

and the F_y channel will read:

$$F_y = W sin(\theta) = 0.0436W \tag{2.2}$$

In this case, F_x registers 99.9% of the signal that it's supposed to, while F_y registers 4.4% of the wrong signal. The main axis calibrates correctly, while it is impossible to tell if the other axis picked up crosstalk or if the sensor is out of alignment.

To actually calibrate for crosstalk, a rigid fixture must be precisely machined to do benchtop crosstalk calibrations. This process would be time consuming and would likely only show that the factory supplied sensitivity matrix is correct.

To take care of crosstalk in all of the experimental data, the factory supplied sensitivity matrix was assumed to be correct and was used when converting the voltage measurements to forces and moments. The diagonal of this matrix was replaced by the calibration done daily on each axis of the sensor. The off diagonal terms, representing the crosstalk terms, were left at the factory values. The values and implementation of this matrix can be seen in the AMTI MC1-6 manual.

2.3.3 Force Rotations

Figure 2-5, from the previous section, shows the sign convention of the dynamometer. The pitch angle (θ) is in the same direction as M_z and the roll angle (ϕ) is in the same

direction as M_y. The dyno's axes, fixed to the pitching and rolling foil shaft, rotate relative to the carriage reference frame. While calculating thrust, lift, and efficiency, the dyno forces must be rotated into the roll frame and into the carriage frame. The roll frame is the frame that moves with the foil as it rolls, but does not move with the pitch motion.

The forces, $\bar{F}$, and moments, $\bar{M}$, in the dyno frame can be rotated into the roll frame by multiplying by the pitch rotation matrix, $\bar{\bar{R}}_\theta$

$$\bar{\bar{R}}_\theta = \begin{vmatrix} cos\theta & -sin\theta & 0 \\ sin\theta & cos\theta & 0 \\ 0 & 0 & 1 \end{vmatrix} \tag{2.3}$$

$$\bar{F}_p = [F_{xp} \ F_{yp} \ F_{zp}] = \bar{\bar{R}}_\theta \bar{F} \tag{2.4}$$

$$\bar{M}_p = [M_{xp} \ M_{yp} \ M_{zp}] = \bar{\bar{R}}_\theta \bar{M} \tag{2.5}$$

Similarly, to transfer these forces and moments into the carriage frame, $\bar{F}_p$ and $\bar{M}_p$ must be multiplied by the roll rotation matrix, $\bar{\bar{R}}_\phi$

$$\bar{\bar{R}}_\phi = \begin{vmatrix} cos\phi & 0 & sin\phi \\ 0 & 1 & 0 \\ -sin\phi & 0 & cos\phi \end{vmatrix} \tag{2.6}$$

$$\bar{F}_c = [F_{xc} \ F_{yc} \ F_{zc}] = \bar{\bar{R}}_\phi \bar{\bar{R}}_\theta \bar{F} = \bar{\bar{R}}_\phi \bar{F}_p \tag{2.7}$$

$$\bar{M}_c = [M_{xc} \ M_{yc} \ M_{zc}] = \bar{\bar{R}}_\phi \bar{\bar{R}}_\theta \bar{M} = \bar{\bar{R}}_\phi \bar{M}_p \tag{2.8}$$

Chapter 3

Measurements

This Chapter shows how the forces measured by the dynamometer are used to calculate power input, power output, efficiency, and center of force of the flapping foil over the range of flapping parameters.

For each run, the following procedure was followed.

1. An iterative solver, in Microsoft Exel, solves for ϕ_o, θ_o, and f from the desired h_o/c, St, and α_{max}

2. The data aquisition is started to record zeros.

3. The carriage is started down the tank.

4. The foil motion is commanded by the Galil user interface using the results from step 1 (note: Starting the motion before there is flow over the foil leads to larger forces, and could damage the dynamometer)

5. The foil motion is stopped.

6. The carriage stops automatically.

7. The data aquisition is stopped, and the data is saved.

8. The carriage is returned to the other end of the tank.

9. Return to step 1.

3.1 Power Input

All of the power input to the system was input through the two electric motors. The power input to these motors could be measured electrically, and this measurement is useful for designing the power system of a flapping foil AUV. However, this power input measurement is dependent on the efficiency of the specific motors used to drive the foil. With the dynamometer mounted on the foil shaft, the power input to the fluid can be measured, independently of the motor characteristics. This power measurement can then be used to calculate the hydrodynamic efficiency of the flapping foil.

The power input in the pitch axis is calculated by multiplying the pitch angular velocity, $\dot{\theta}(t)$ by the applied pitch moment, M_{pitch}.

$$P_{in,pitch} = M_{pitch}\dot{\theta} \tag{3.1}$$

$$M_{pitch} = -M_z \tag{3.2}$$

$$P_{in,pitch} = -M_z\dot{\theta} \tag{3.3}$$

The measured pitch moment, M_z, is equal in magnitude, but opposite in sign to the applied pitch moment.

The power input in the roll axis is calculated similarly by multiplying roll angular velocity, $\dot{\phi}(t)$, by the applied roll moment, M_{roll}.

$$P_{in,roll} = M_{roll}\dot{\phi} \tag{3.4}$$

$$M_{roll} = F_{xp}R_o - M_{yp} \tag{3.5}$$

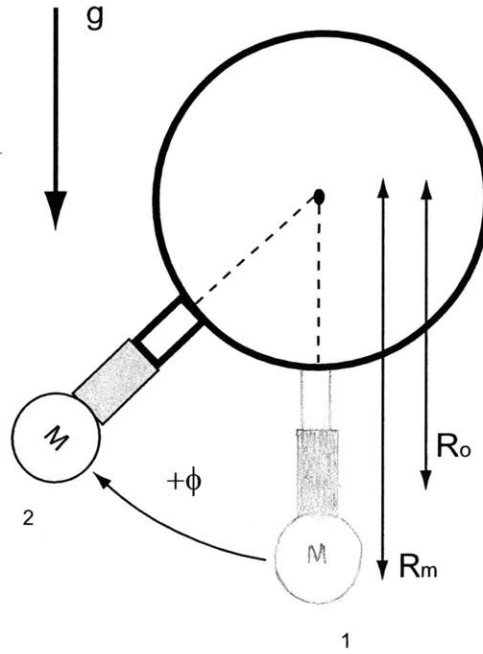$$P_{in,roll} = (F_{xp}R_o - M_{yp})\dot{\phi} \tag{3.6}$$

Figure 3-1: Front view of the module with the weight attached for power verification tests

where R_o is the distance from the center of roll to the center of the dynamometer, and the definition of M_{roll} can be derived from a simple static beam force and moment balance.

The total power input to the foil is then defined as the addition of these two power measurements.

$$P_{in} = P_{in,roll} + P_{in,pitch} \tag{3.7}$$

3.1.1 Power Input Verification

To verify the power input measurements and calculations, some simple experiments were performed to measure the power required to lift a weight a specified distance.

Figure 3-1 shows a diagram of an end on view of the module with a 0.45kg mass attached. The total weight measured by the sensor was M=0.486kg; the 0.45kg mass plus the 0.036kg sensor head. R_m is the distance from the center of roll to the center

39

ϕ_o (degrees)	PE_2 (J)	KE_1 (J)	W_{calc} (J)	$\overline{P}_{calc}$ (Watts)
45°	0.344	0.023	0.321	0.321
55°	0.501	0.034	0.467	0.467
65°	0.678	0.047	0.631	0.631

Table 3.1: Results of energy calculations for a quarter period of motion of a sinusoid with frequency of 0.25 Hz and a range of roll amplitudes

of the total mass. Position 1 marks the bottom of a cycle, and position 2 marks the peak of a cycle.

Theoretical Calculations

The weight was oscillated in a sinusoidal motion, with position $\phi(t) = \phi_o sin(\omega t)$ and velocity $\dot{\phi} = \phi_o \omega cos(\omega t)$. It was oscillated in air so the drag is considered negligible and all of the input energy must come through the dynamometer. At position 1 it has no potential energy, $PE_1 = 0$, and a kinetic energy of $KE_1 = \frac{1}{2}M(\phi_o \omega R_m)^2$. At position 2 it has no kinetic energy, $KE_2 = 0$, and a potential energy of $PE_2 = Mg(R_m - R_m cos\phi_o)$. The energy balance of the system:

$$PE_1 + KE_1 + W_{calc} = PE_2 + KE_2 \tag{3.8}$$

simplifies to:

$$W_{calc} = PE_2 - KE_1 \tag{3.9}$$

$$W_{calc} = Mg(R_m - R_m cos\phi_o) - \frac{1}{2}M(\phi_o \omega R_m)^2 \tag{3.10}$$

where, W_{calc} is the theoretical, calculated work input.

The average power applied to raise the weight, P_{calc} is then W_{calc} divided by the time it took to raise the weight, τ.

$$\overline{P}_{calc} = \frac{W_{calc}}{\tau} \tag{3.11}$$

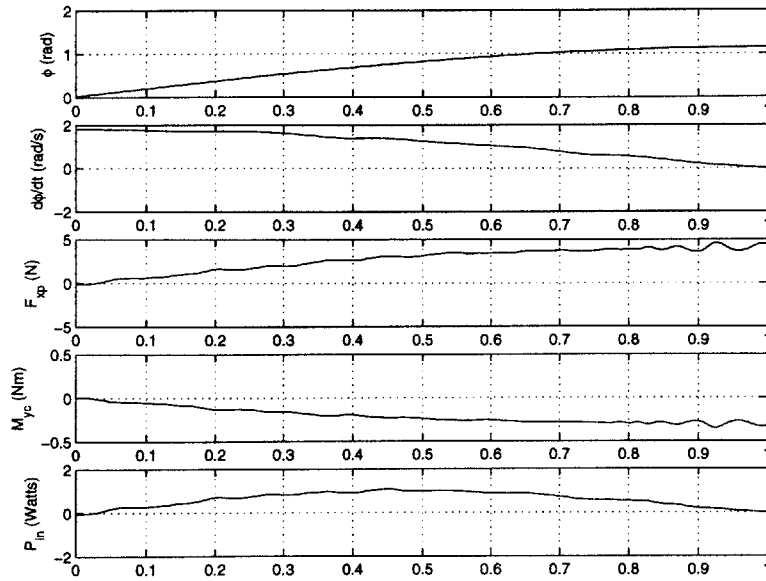Table 3.1 shows the results of equation 3.11 for three different roll amplitudes.

40

Figure 3-2: The signals used to calculate the power input needed to oscillate the weight with f=0.25Hz and $\phi_o = 65°$

The numerical values of energy and power are equal because the time, τ, of a quarter cycle is 1s.

Experimental Results

The above calculations were made to verify the average power output measured by the dynamometer while performing a similar motion. In some cases, the weight was also oscillated about the pitch axis with an amplitude of $\theta(t) = \theta_o cos(\omega t)$. This oscillation should not affect the roll power results because the weight is symmetric about the pitch axis and is not oscillated fast enough to cause any gyroscopic effects. These pitch oscillations were introduced to check the force rotations presented in Section 2.3.3.

Figure 3-2 shows all of the signals used to calculate the power input over a quarter period of motion.The angular position, $\phi(t)$, was measured directly from the potentiometer. The angular velocity, $\dot{\phi}(t)$, is the time derivative of the position. The applied force and moment, F_{xp} and M_{yc}, are the direct outputs of the dynamometer for the non-pitching cases, and the transformation of the dynamometer output for

$\phi_o(degrees)$	$\theta_o(degrees)$	$\overline{P}_{exp}$ (Watts)	$\overline{P}_{calc}$(Watts)	$\%_{diff}$
45	0	0.327	0.321	1.8%
55	0	0.472	0.467	1.0%
65	0	0.640	0.631	1.4%
65	5	0.580	0.631	−8.1%
65	25	0.602	0.631	−4.6%
65	45	0.629	0.631	−0.3%

Table 3.2: Results of experiments to verify average power measurements.

the pitching cases. The power input, $P_{in}(t)$, is calculated from equation 3.6.

Table 3.2 shows the experimental results for 6 different actuation cases and compares them to the theoretical calculations. Each experiment was performed twice and the average taken. The results for the non-pitching cases all had an error of less than two percent. These results show that the dynamometer is working properly and that the equations for calculating power input are implemented correctly.

The results for the pitching cases show a much greater discrepancy of up to eight percent from the expected value. These errors were likely caused by errors in the pitch position estimation and are discussed in section 5.2.1

3.1.2 Power Input Measurement

For flapping foil runs, the power input was calculated by transforming the dynamometer measurements into the appropriate forces and moments and then using equations 3.3 and 3.6 to calculate the power input to each axis.

Figure 3-3 shows the signals used to calculate the power input to the pitch axis for a single run. $\theta(t)$ is the phase shifted and amplitude scaled potentiometer signal, $\dot{\theta}(t)$ is the time derivative of this signal, $M_z(t)$ is an output of the dynamometer, and $P_{in}(t)$ is calculated from equation 3.3.

As shown in Figure 3-3, the power input to the pitch axis is not always positive. In a non-rolling case, the power would always be positive because the angular velocity and applied moment are always of the same sign. However, the roll motion causes fluid forces on the foil that result in applied moments that are sometimes opposite in direction to the motion. In most of the cases analyzed, the mean pitch input power
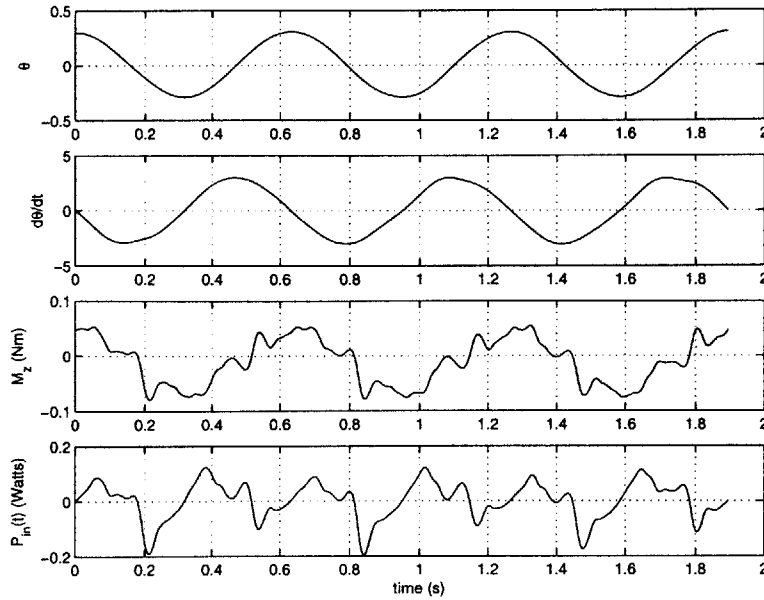
Figure 3-3: The signals used to calculate the power input in the pitch axis for a run of $h_o/c = 1.5, St = 0.5, and\,\alpha_{max} = 40°$

is insignificant when compared to the mean roll input power, but it is always added into the final calculation of power.

Figure 3-4 shows the signals used to calculate the power input to the roll axis. $\phi(t)$ is measured directly from the potentiometer, $\dot{\phi}(t)$ is the numerical time derivative of $\phi(t)$, F_{xp} and M_{yp} are the forces and moments transformed into the roll frame, and P_{in} is calculated from equation 3.6. In all of the analyzed cases, $P_{in,roll}$ is always positive and has a much larger mean than the pitch input power.

Figures 3-5 through 3-7 show the time averaged power input results for all experiments run at the three different heave amplitudes. It is clear from these figures that the power input increases with St and α_{max}, and decreases with h_o/c.

The majority of the power input comes from the roll motion, so the behavior of the $\overline{P}_{in}$ curves can be explained by examining the lift force, F_{xc}, on the foil. This force increases with St and α_{max} because the foil has a higher maximum roll velocity and a higher angle of attack to the flow. This increased lift force leads to higher power input values.
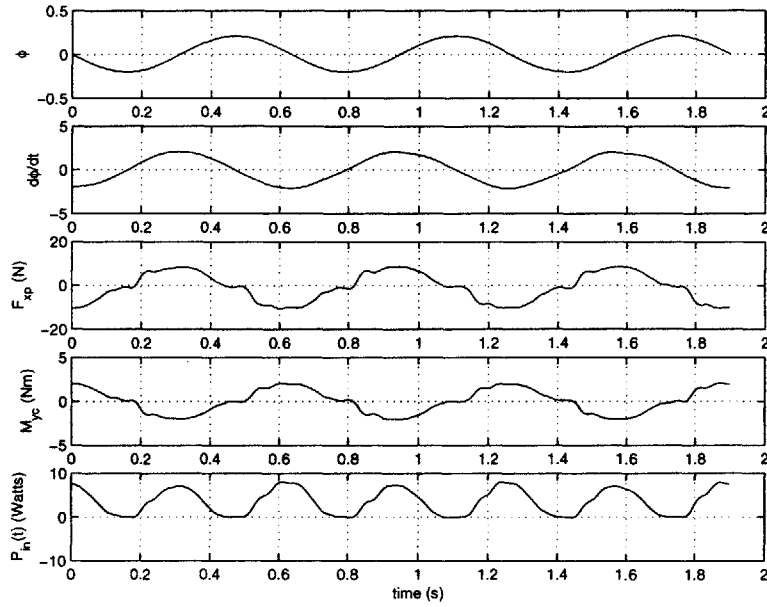
43

Figure 3-4: The signals used to calculate the power input in the roll axis for a run of $h_o/c = 1.5$, $St = 0.5$, and $\alpha_{max} = 40°$
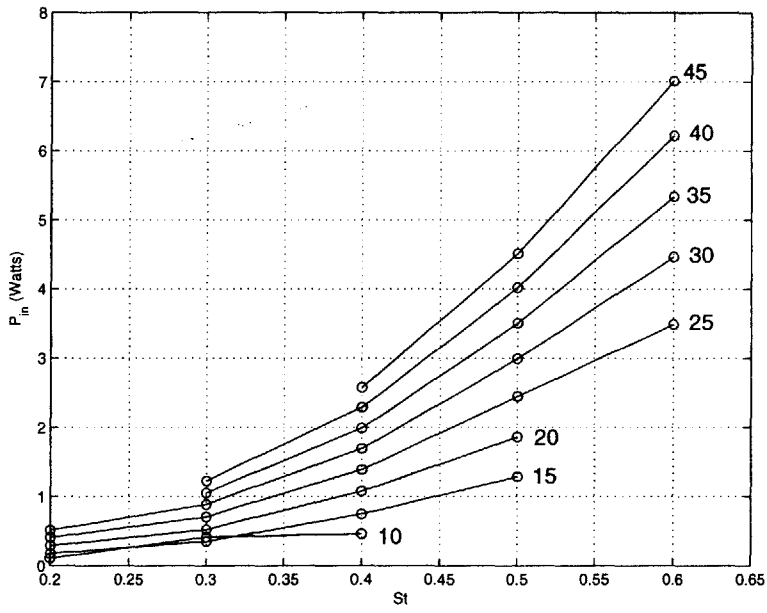

Figure 3-5: $\overline{P}_{in}$ results for $h_o/c = 1$. The numbers along the right represent α_{max} in degrees.
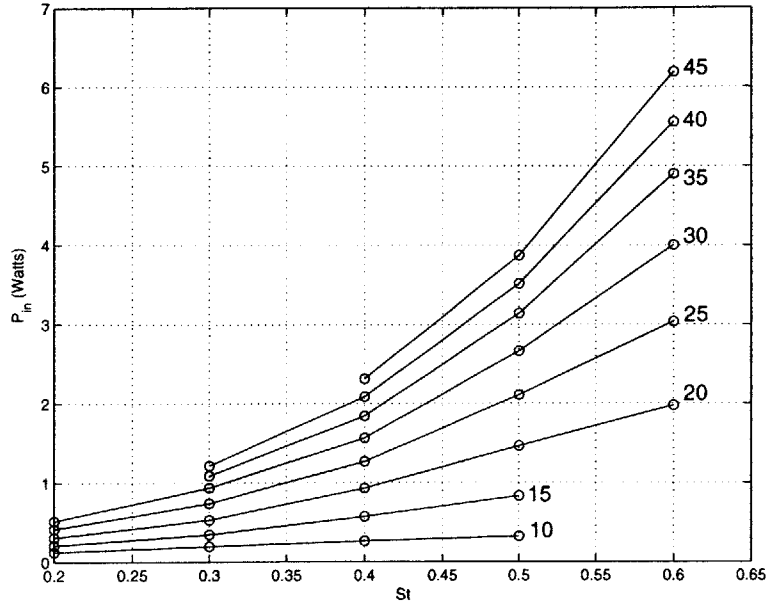
Figure 3-6: $\overline{P}_{in}$ results for $h_o/c = 1.5$. The numbers along the right represent α_{max} in degrees.
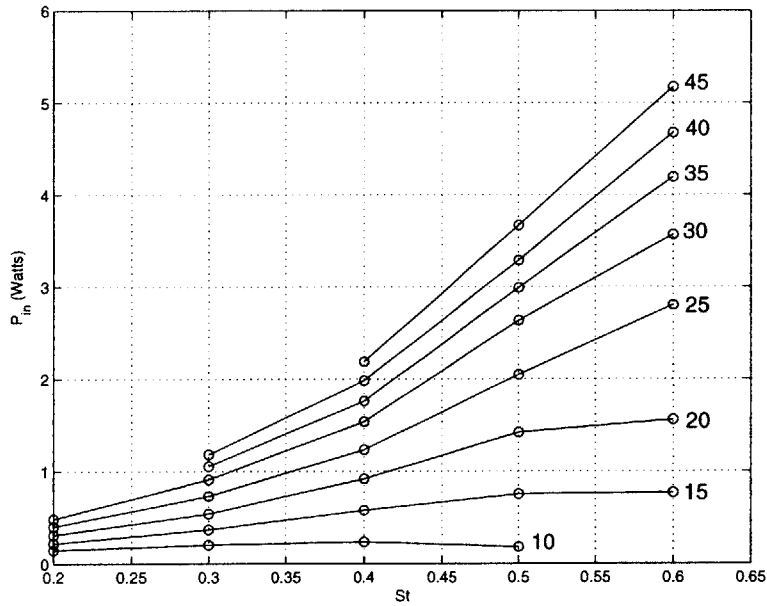

Figure 3-7: $\overline{P}_{in}$ results for $h_o/c = 2$. The numbers along the right represent α_{max} in degrees.

45

No error bars are shown in the plot because the standard deviation, taken of six to eight repeated runs at various points always came to less than 1% of the mean. This small error would not show up on the plot. The error analysis will be discussed further in Chapter 5.

3.2   Power Output

The time averaged power output of the foil is defined as the time averaged thrust multiplied by the flow velocity. This result would be the useful power output if the foil module were mounted on a flapping foil vehicle.

$$\overline{P}_{out} = \overline{T}U \qquad (3.12)$$

$$\overline{T} = -\overline{F}_{yc} \qquad (3.13)$$

$$\overline{P}_{out} = -\overline{F}_{yc}U \qquad (3.14)$$

Figures 3-8 through 3-10 show the time averaged power output results for all experiments run at the three different heave amplitudes. In most cases, the data follows a similar trend as the $\overline{P}_{in}$ results, increasing with St and α_{max}, and decreasing with h_o/c. At high St and low α_{max}, the power output drops off because of the bad angle of attack profiles near the foil's root. To see clearer trends in the data, the plots of C_T in section 4.1 should be studied. These data are discussed in more detail in section 4.1.

The errorbars, again, are present on the power output plots, but too small to see because of the small scale of the y-axes. The magnitudes of these errors are presented in Chapter 5.
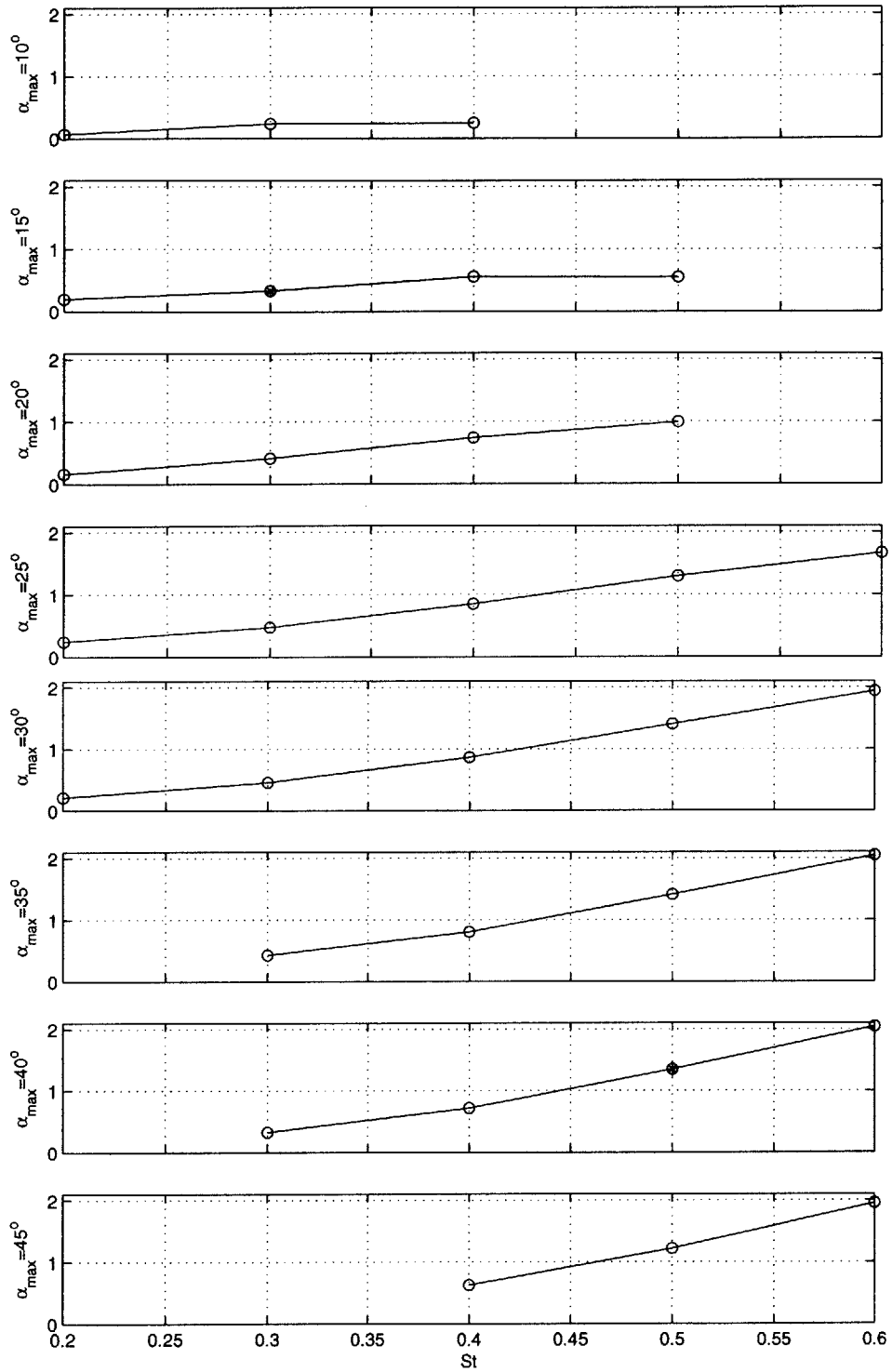
46

Figure 3-8: $\overline{P}_{out}$ results for $h_o/c = 1$. Each subplot represents a different α_{max}, and the vertical axes are in Watts.

Figure 3-9: $\overline{P}_{out}$ results for $h_o/c = 1.5$. Each subplot represents a different α_{max}, and the vertical axes are in Watts.
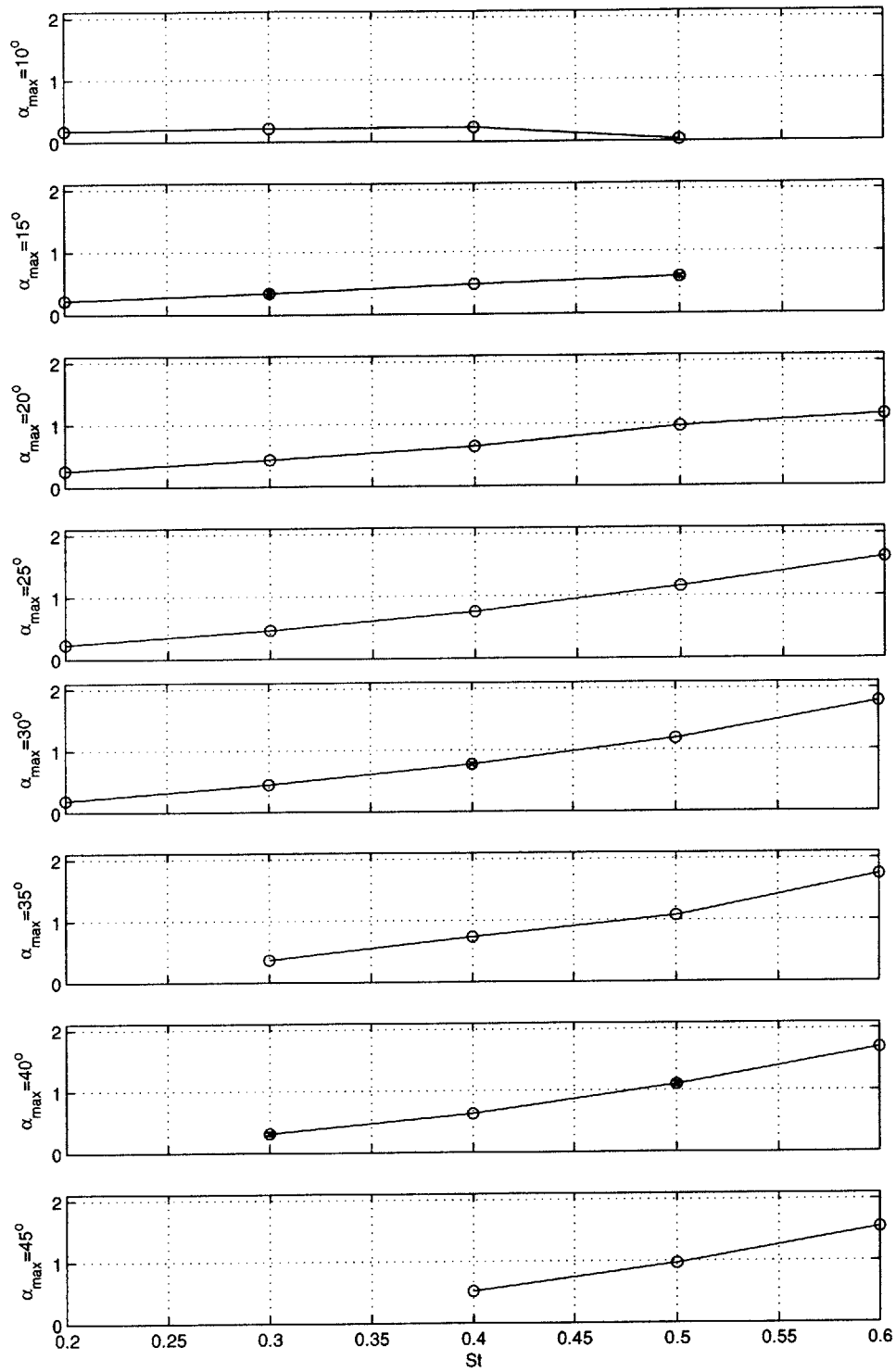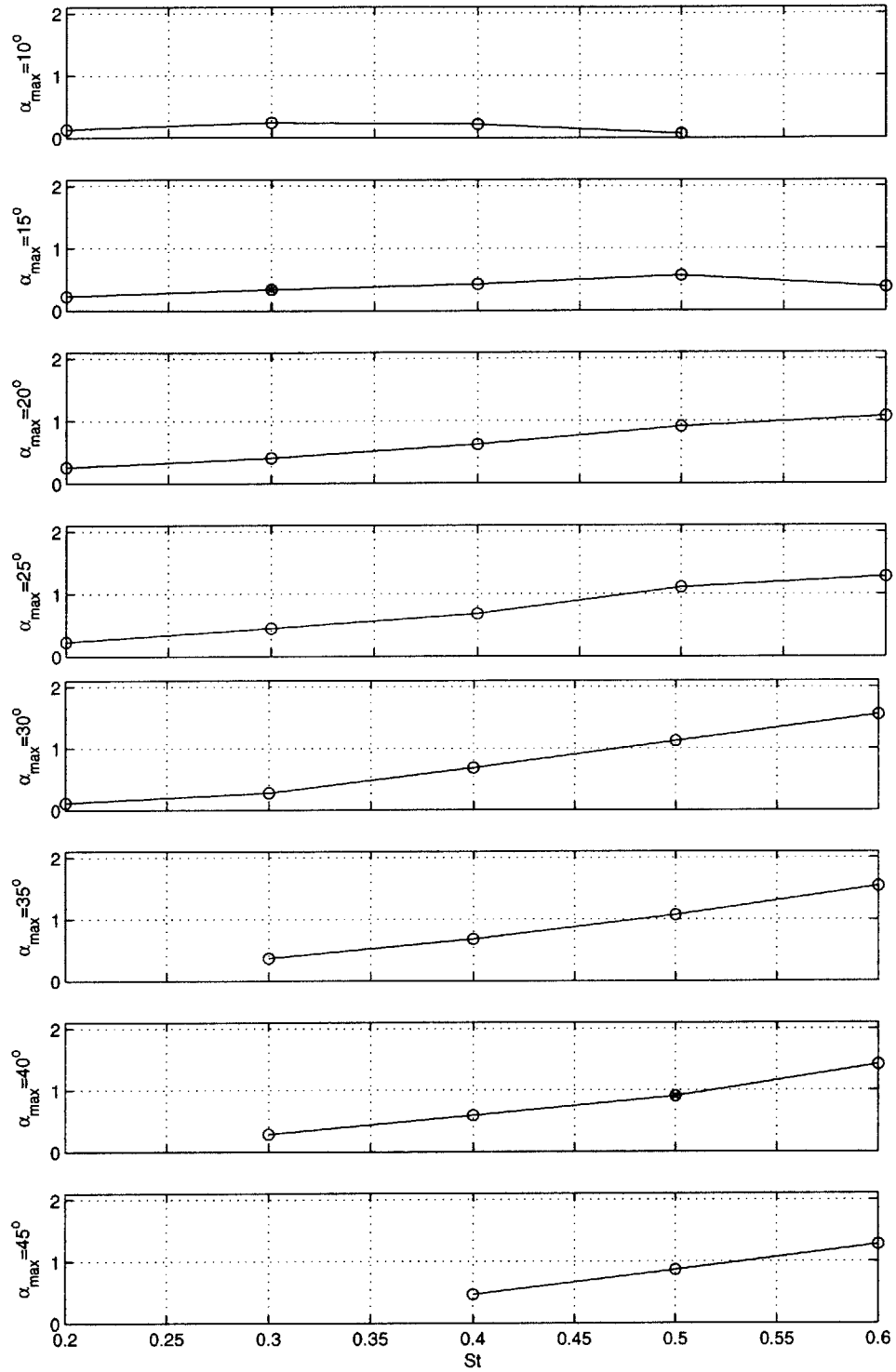
Figure 3-10: $\overline{P}_{out}$ results for $h_o/c = 2$. Each subplot represents a different α_{max}, and the vertical axes are in Watts.

3.3 Center of Force

In all previous three-dimensional flapping foil literature, the center of force of the flapping foil, R_{cf}, was assumed to be at the 70% span of the foil.

$$R_{cf} = R_{0.7} = R_r + 0.7S \qquad (3.15)$$

Where R_r is the distance from the center of roll to the foil root (the "hub") and S is the foil span.

This assignment of the center of force was based off of the center of force of an elliptically loaded propeller, which occurs at 70% of the propeller radius ($0.7 * D/2$, where D is propeller diameter). Note that for a flapping foil the center of force convention depends on the radius of the hub, while for a propeller the convention depends only on the overall radius of the blade.

With the dynamometer positioned on the shaft, it is simple to calculate the center of force by dividing the moment measurement by its corresponding force measurement.

$$R_{cf} = R_o + M_y/F_x \qquad (3.16)$$

M_y and F_x were chosen for this calculation because they are the dominant moment and force acting on the foil.

Figure 3-11 shows a timetrace of M_y/F_x for a single run. At the peaks of the roll motion F_x and M_y approach zero, so noise and numerical errors cause the calculation to oscillate between infinity and negative infinity. However, for about half of each cycle, the distance measurement levels out to a steady value. The mean of this value can be used to calculate an average percent of the span, measured from the root, that the force acts on.

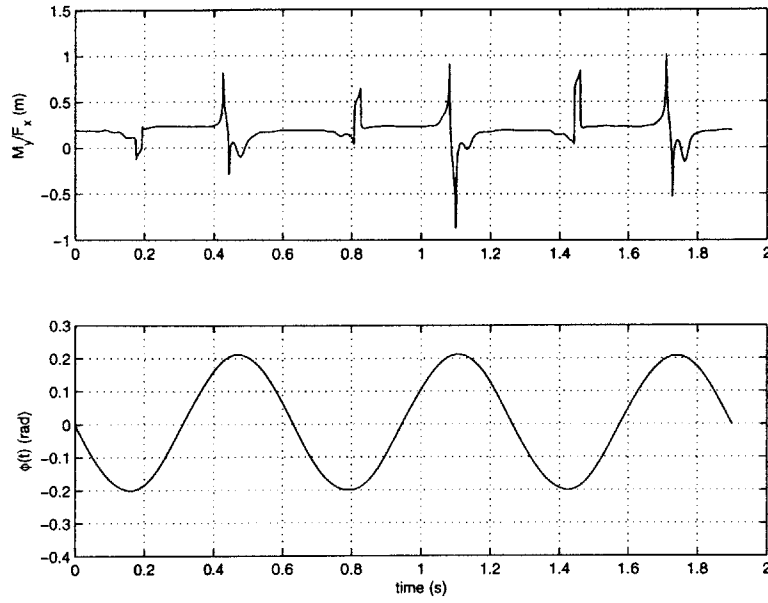$$\%span = \frac{100(R_{cf} - R_r)}{S} \qquad (3.17)$$

Figure 3-11: The distance to the center of force on the foil from the center of the dynamometer and the timetrace of the roll position for a run of $h_o/c = 1.5, St = 0.5, and \alpha_{max} = 40°$

$$\%span = \frac{100(R_o + \overline{M_y/F_x} - R_r)}{S} \qquad (3.18)$$

Chapter 4

Results and Discussion

This chapter presents the thrust, efficiency, and center of force results.

4.1 Thrust

Measuring the thrust of the three-dimensional flapping foil and comparing these results to previous work was the first goal of the thesis.

To compare the thrust results to previous experiments, the thrust measurements had to be non-dimensionalized into the thrust coefficient, C_T.

$$C_T = \frac{-\overline{F_{yc}}}{\frac{1}{2}\rho U^2 c_{av} S},$$ (4.1)

Figures 4-1 through 4-3 plot the thrust coefficient contours for the three heave amplitudes tested. The diamonds on the grid represent data points, and the location of the circles mark data points that were repeated to calculate standard deviation and error. The area of the circles correspond to the standard deviation divided by the mean at that point. The exact error represented by each circle is presented in chapter 5.

The contours are made up of the same data as the $\overline{P}_{out}$ results of section 3.2, so they follow the same behavior of increasing with St and α_{max}, and decreasing with h_o/c.
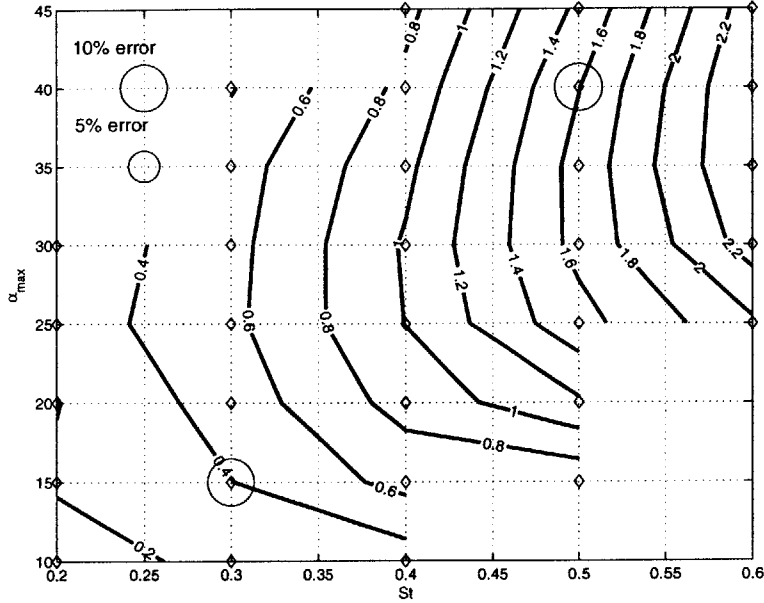
Figure 4-1: C_T results for $h_o/c = 1$. The circles' areas scale with percent error.

The contour plots compare well to the results of Read, Flores, and Polidoro [12] [2] [9]. Figure 4-1, the C_T plot of $h_o/c = 1$ has a minimum of $C_T = 0.2$ at St=0.2 and $\alpha_{max} = 10°$. It then increases diagonally upwards to a peak of $C_T = 2.2$ at St=0.6 and $\alpha_{max} = 30°$. Read's plot of $h_o/c = 1$ follows the exact same pattern.

Figure 4-2, the C_T plot of $h_o/c = 1.5$, has contours of the same shape, but they have a minimum of $C_T = 0.4$ and a maximum of $C_T = 2$. Flores' data for $h_o/c = 1.5$ peaks with a C_T of 1.1 instead of 2. Polidoro's data for the same kinematics (0.3m span foil and an $h_o/c = 1.4$) peaks at a C_T of 1.75.

4.2 Efficiency

The hydrodynamic efficiency of the foil is defined as the power output divided by the power input.

$$\eta = \frac{P_{out}}{P_{in}} \tag{4.2}$$

Figures 4-4 through 4-6 plot the efficiency contours for the three heave amplitudes tested. The efficiency values at low St and α_{max} are unreliable because of the large
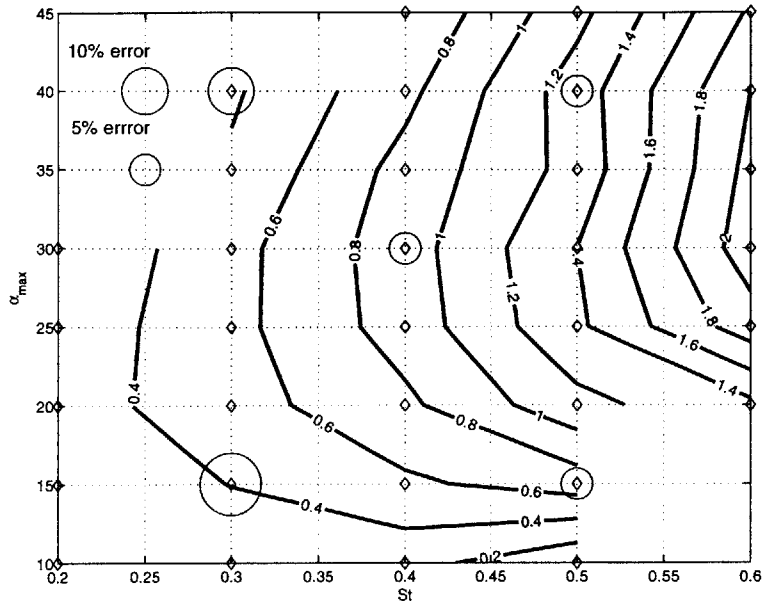
54

Figure 4-2: C_T results for $h_o/c = 1.5$. The circles' areas scale with percent error.
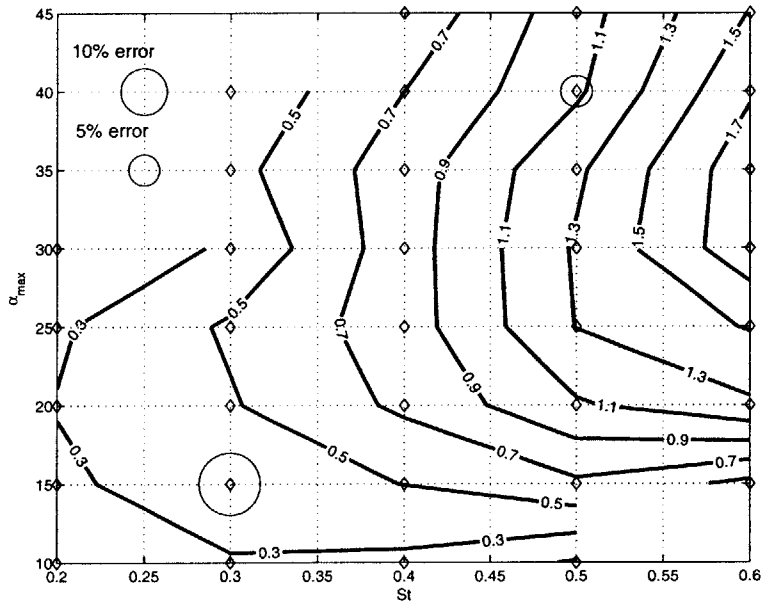

Figure 4-3: C_T results for $h_o/c = 2$. The circles' areas scale with percent error.
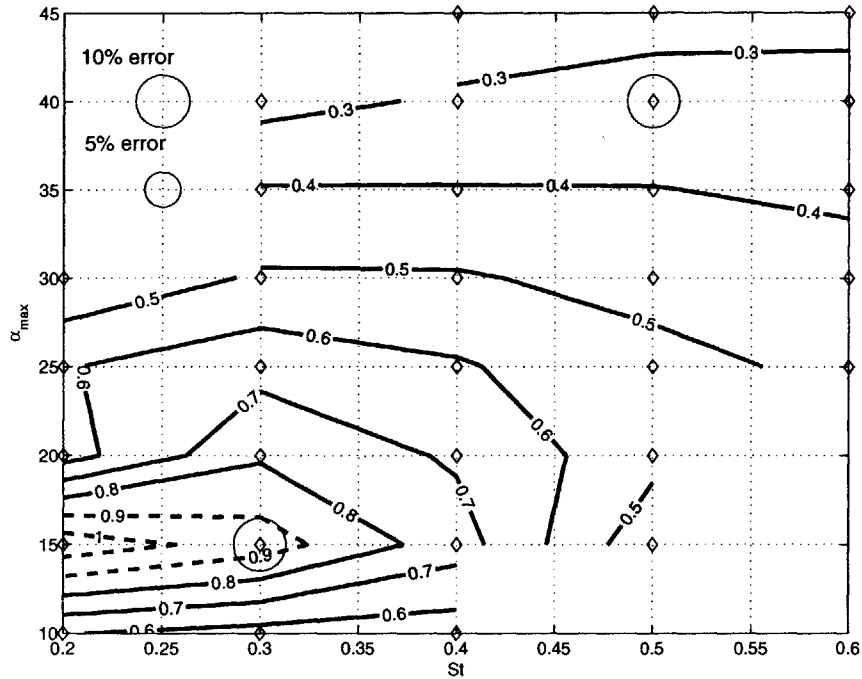
Figure 4-4: η results for $h_o/c = 1$. The circles' areas scale with percent error, and the dashed lines represent unreliable data.

errors associated with these low thrust regions. However, the general shape of the contours should reflect the efficiency behavior. All three plots show a peak of efficiency at $\alpha_{max} = 15^o$ and at low strouhal numbers. The peak at $\alpha_{max} = 15^o$ and low St corresponds exactly with Read's results. However, he was able to resolve lower thrust forces, and his peaks are better defined and do not surpass an efficiency of 0.7.

4.3 Center of Force

The center of force value is calculated by dividing the measured moment, M_y, by the measured force, F_x. It is helpful to present this distance as a percentage of the foil span from the foil root. With this representation, it can be compared to the assumed value of 70%.

Figures 4-7 through 4-9 show the $\%S$ results for all of the runs above $\alpha_{max} = 15$. The lower angle of attack runs are not included because the error is too great. Center

Figure 4-5: η results for $h_o/c = 1.5$. The circles' areas scale with percent error, and the dashed lines represent unreliable data.

of force decreases with α_{max} and h_o/c. It is constant in St for low α_{max}, but has a peak at $St \approx 0.4$ for higher α_{max}. None of the runs reach the assumed center of force of 70% of the span. Instead they all range between 47% and 69% of the span.
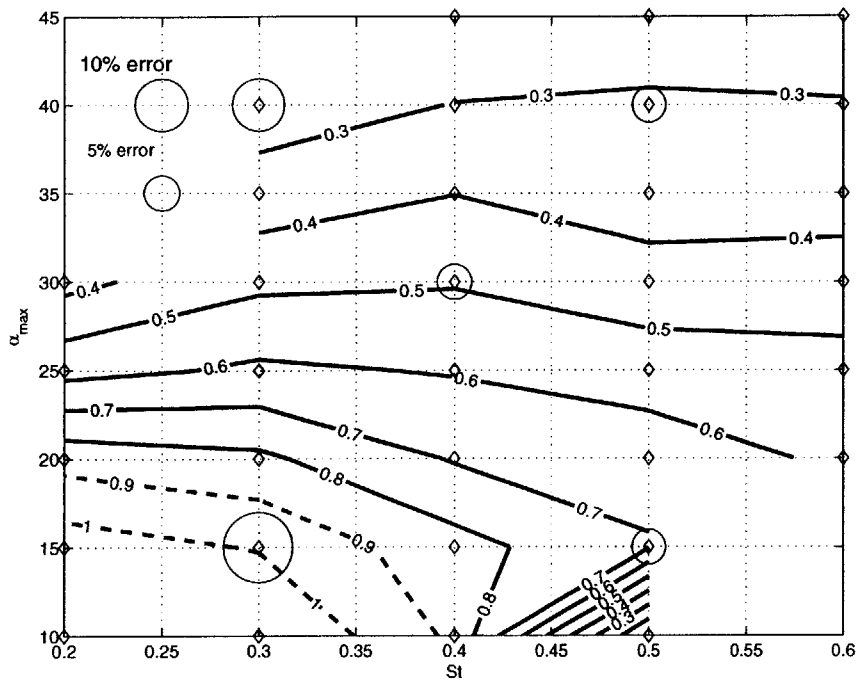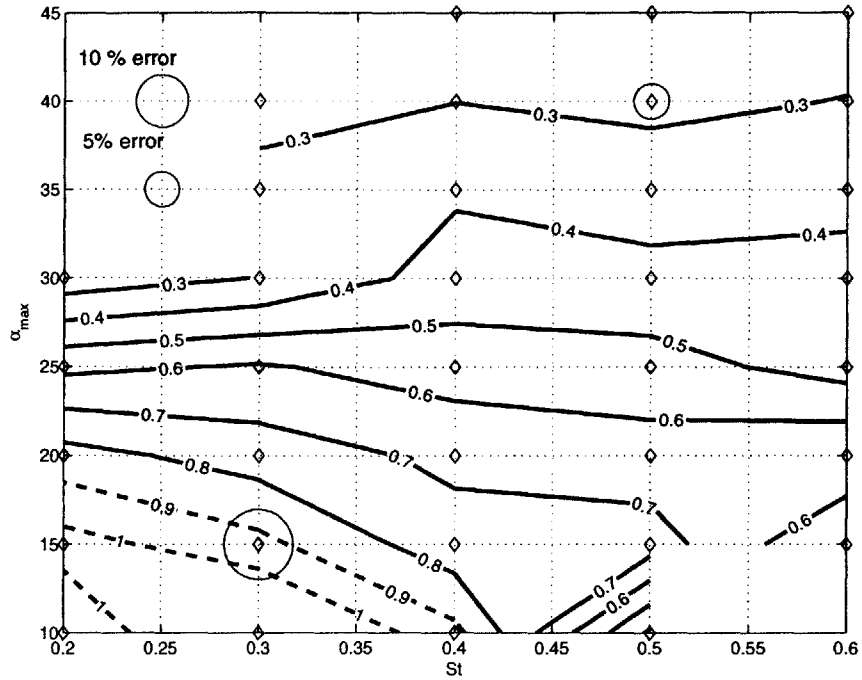
Figure 4-6: η results for $h_o/c = 2$. The circles' areas scale with percent error, and the dashed lines represent unreliable data.
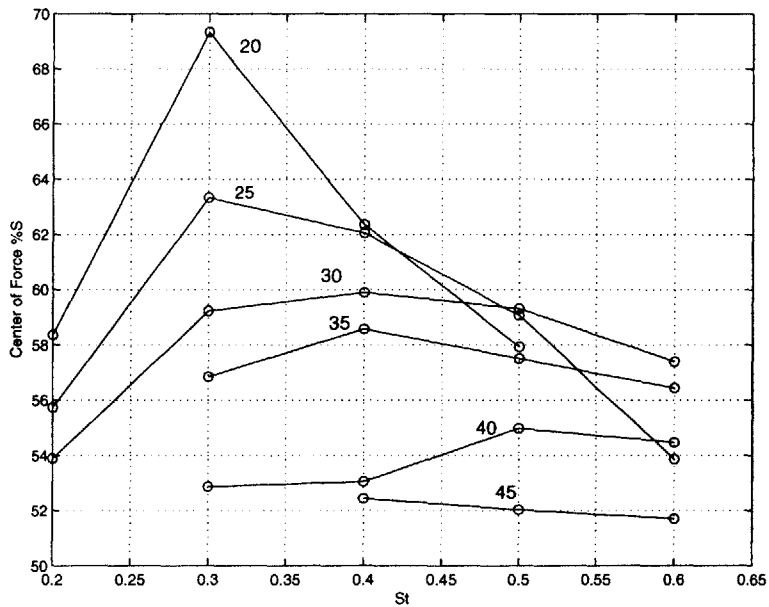

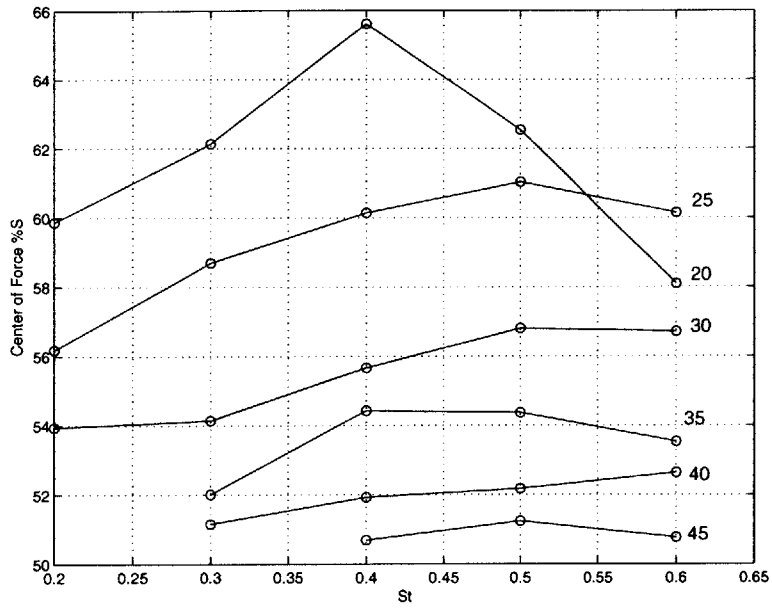Figure 4-7: $\%S$ results for $h_o/c = 1$
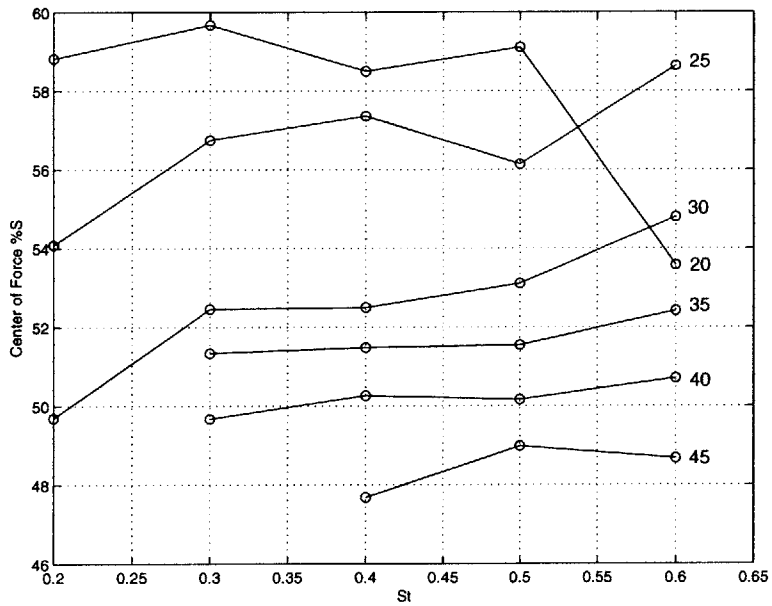
Figure 4-8: %S results for $h_o/c = 1.5$

Figure 4-9: %S results for $h_o/c = 2$

Chapter 5

Error Analysis

5.1 Repeatability

To ensure that the results were repeatable and to find the standard deviation of the results, nine sets of repeated runs were performed.

For $h_o/c = 1.5$, five sets of six repeated runs were performed, while for $h_o/c = 1$ and $h_o/c = 2$, two sets of six repeated runs were performed. The percent that the standard deviation varies from the mean for all of the repeated runs is presented in table 5.1.

For all cases, the power output measurement has significantly more error than the power input measurement. This error is greater for the low thrust runs than the high thrust runs. By analyzing the repeatability of each force measurement, it was found that all of this error comes from the F_{yc} force, which is used to calculate both P_{out} and C_T, but does not significantly affect the calculation of P_{in}.

The P_{in} measurement has a repeatability error of less than 1% for all repeated runs. It is calculated from the larger lift forces and moments, which have much less susceptibility to angular misalignments than the thrust calculations.

Finally, the repeatability error for the efficiency is very similar to that of the P_{out} error because P_{out} is used in the efficiency calculation.

h_o/c	St	α_{max}	♮ of Runs	P_{out} or C_T	P_{in}	η
1.5	0.3	15	8	18.2%	0.9%	18.7%
1.5	0.5	15	6	4.4%	3.6%	3.0%
1.5	0.4	30	6	2.5%	0.28%	2.6%
1.5	0.3	40	6	8.6%	0.66%	8.7%
1.5	0.5	40	8	3.8%	0.33%	4.1%
1	0.3	15	6	9.9%	0.67%	10.1%
1	0.5	40	6	8.79%	0.83%	9.8%
2	0.3	15	6	11.5%	0.47%	11.8%
2	0.5	40	6	4.0%	0.52%	4.4%

Table 5.1: Percent error from mean of a standard deviation for all repeated runs.

5.2   Sources of Error and Solutions

5.2.1   Angular Misalignments

Angular misalignments in the pitch axis are caused by the 2.5^o backlash in the pitch gearhead and the possible 2° error in the pitch position estimation. These misalignments cause the dynamometer to be up to 4.5^o out of its desired alignment.

The calculation of the thrust force is highly susceptible to pitch misalignments because it is calculated from the addition of the sine of a large force, F_x, and cosine of a small force, F_y. As described in section 2.3.2 this leads to large force errors if there is a small error in the angle.

$$F_{yc} = F_x sin\theta + F_y cos\theta \tag{5.1}$$

In the low thrust cases, the thrust calculation is dominated by the error in the $F_y cos\theta$ term and fluctuations in θ cause fluctuations in F_{yc}.

To reduce the effect of pitch angular misalignments, a potentiometer must be installed on the pitch axis. Also, to eliminate the error, a pitch motor with no backlash must be used.

The above steps reduce the pitch error from the zero position. However, to make these steps worthwhile, the zero position must be correct. The module must be aligned properly to the flow, the dynamometer aligned properly to the module, and

the foil aligned properly to the dynamometer. To align the module properly to the flow, its mount to the water tunnel window or towtank carriage must be precisely machined. To align the dynamometer to the module and the foil to the dynamometer, alignment pins should be used at all couplings. The potentiometers on the pitch and roll axes can then consistently return the foil to a zero position with very little error in its alignment to the flow.

5.2.2 Crosstalk

Any crosstalk that is not accounted for in the factory sensitivity matrix would lead to errors in the force measurements.

As described in section 2.3.2, it would be difficult to measure the crosstalk of the dynamometer, and the factory supplied matrix is probably sufficient. However, crosstalk is not a completely linear phenomenon and the crosstalk sensitivity matrix is different for every possible combination of applied forces and moments.

Based on the measurements taken already by the dynamometer, the range of forces produced by the flapping foil is known. If a sensitivity matrix is developed for this specific range of forces, then it will lead to more accurate results than the factory matrix.

Chapter 6

Conclusions

The purpose of this project was to implement and validate a new force sensor, measure the hydrodynamic efficiency of a three-dimensional flapping foil, and measure the center of force of a three-dimensional flapping foil. For each of the goals, a conclusion was drawn.

- The thrust coefficients measured by the dynamometer compare well to previous results, and the sensor should be used in future experiments.

- The hydrodynamic efficiency was measured reliably in high thrust cases, however improvements must be made to the experimental apparatus to measure efficiency in low thrust cases.

- The center of force assumption of 70% of the span is slightly higher than the actual value ranging between 47% and 69% of the span.

The AMTI dynamometer, mounted directly on the foil shaft, is ideal for investigating the performance of three-dimensional flapping foils. Its calibration was always linear, and always within 3% of expected values. It measured the power needed to oscillate a weight to within 2% of the expected value. If the pitch angle were reliably measured, then the dynamometer would have likely made repeatable efficiency measurements for the very low thrust cases.

Despite the errors in the low thrust runs, the efficiency results follow the same pattern as previous results. The efficiency peaks at a maximum angle of attack of 30° and at low Strouhal Numbers.

By putting the dynamometer as close to the foil as possible, all power losses due to gear friction, shaft seal friction, etc. can be ignored; reducing power losses and improving measured efficiency. However, for these tests, the efficiency measured should still not approach 1. The drag of the foil and foil couple, the weight of the foil and foil couple, and the surface effects are all significant power losses, and reduced the actual efficiency. Once the efficiency can be reliably measured, it must be optimized by adjusting foil geometry, foil flexibility, and angle of attack profiles.

The center of force measurements are useful for both the design and control of flapping foil vehicles because without an accurate center of force measurement an accurate moment estimation can not be made. Moment estimates are important when sizing motors and bearings, and while developing the control systems of flapping foil vehicles. The center of force measurements presented in this thesis are for a specific foil and for a limited range of kinematics. This data is not sufficient evidence to change the convention used in all of the dimensionless numbers and in moment estimates. Further investigations should be made with different foils and a broader range of kinematics.

6.1   Future Work

To make flapping foil vehicles capable of completing long missions, the efficiency of flapping foils must be understood and optimized. Future investigations into the efficiency of three-dimensional flapping foils will involve optimizing both the hydrodynamic efficiency of the foil and the efficiency of the motors that drive the foil. The hydrodynamic efficiency can be optimized by making the improvements suggested in Chapter 5 and by measuring efficiency for a large range of kinematics, foil geometry, and foil flexibility. The motor efficiency can be improved with the use of rotational springs. Rotational springs store and return the energy of oscillating motions with

very high efficiency, while electric motors oscillate with very poor efficiency. In the future, alternative actuators, using artificial muscles for the oscillating motions, may be more efficient than traditional actuators.

Bibliography

[1] J. Anderson. *Vorticity Control for Efficient Propulsion*. Phd thesis in oceanographic engineering, Massachusetts Institute of Technology, MA, February 1996.

[2] M. Flores. Flapping motion of a three dimensional foil for propulsion and maneuvering of underwater vehicles. Master of science in ocean engineering, Massachusetts Institute of Technology, MA, May 2003.

[3] A. Suleman G. Pedro and N. Djilali. A numerical study of the propulsive efficiency of a flapping hydrofoil. *Int. J. Numer. Meth. Fluids*, 42, 2003.

[4] O. Haugsdal. Motion control of oscillating foils for steady propulsion and starting maneuvers. Master of science in ocean engineering, Norwegian University of Science and Technology and Massachusetts Institute of Technology, MA, December 2000.

[5] N. Kato. Control performance in horizontal plane of a fish robot with mechanical pectoral fins. *IEEE Journal of Oceanic Engieering*, 25, 2000.

[6] C. Martin. Design and performance evaluation of a biomimetic flapping foil. Master of science in ocean engineering, Massachusetts Institute of Technology, MA, June 2001.

[7] J.H. Ostrom. *A History of Vertebrate Sucess*. Jones and Bartlett, Boston, 1992.

[8] F. Hover P. Prempraneerach and M. Triantafyllou. The effect of chordwise flexibility on the thrust and efficiency of a flapping foil. *Journal of Fluids and Structures*, pending.

[9] V. Polidoro. Flapping foil propulsion for cruising and hovering autonomous underwater vehicles. Master of science in ocean engineering, Massachusetts Institute of Technology, MA, May 2003.

[10] R. Rammamurti and W. Sandberg. A three-dimensional computational study of the aerodynamic mechanisms of insect flight. *The Journal of Experimental Biology*, 205, 2002.

[11] P.S.K. Lai R.C. McGregror and N.Bose. Experimental investigations of oscillating foil propellers. *22nd American Towing Tank Conference, ATTC Conference, St. Johns*, August, 1989.

[12] D. Read. Oscillating foils for propulsion and maneuvering of ships and underwater vehicles. Master of science in naval architecture and marine engineering, Massachusetts Institute of Technology, MA, February 1999.

[13] M. Flores F. Hover S. Licht, V. Polidoro and M. Triantafyllou. Design and projected performance of a flapping foil auv. *13th Intern. Symposium on Unmanned Untethered Submersible Technology. Durham, NH*, 2003.